University of New Mexico
UNM Digital Repository

Electrical and Computer Engineering ETDs | Engineering ETDs

9-4-2013

Design, growth and optimization of 2-μm InGaSb/AlGaSb quantum well based VECSELs on GaAs/AlGaAs DBRs.

Pankaj Ahirwar

Follow this and additional works at: https://digitalrepository.unm.edu/ece_etds

Recommended Citation
Ahirwar, Pankaj. "Design, growth and optimization of 2-μm InGaSb/AlGaSb quantum well based VECSELs on GaAs/AlGaAs DBRs.." (2013). https://digitalrepository.unm.edu/ece_etds/6

This Dissertation is brought to you for free and open access by the Engineering ETDs at UNM Digital Repository. It has been accepted for inclusion in Electrical and Computer Engineering ETDs by an authorized administrator of UNM Digital Repository. For more information, please contact disc@unm.edu.

Pankaj Ahirwar

Candidate

Electrical and Computer Engineering

Department

This dissertation is approved, and it is acceptable in quality and form for publication:

Approved by the Dissertation Committee:

Dr. Ganesh Balakrishnan , Chairperson

Dr. Sanjay Krishna

Dr. Kevin J. Malloy

Dr. Thomas J. Rotter

Design, Growth and Optimization of 2-μm InGaSb/AlGaSb quantum well based VECSELs on GaAs/AlGaAs DBRs.

by

Pankaj Ahirwar

B. Tech. (Electrical Engineering), Indian Institute of Technology, Roorkee, India, 2005

DISSERTATION

Submitted in Partial Fulfillment of the
Requirements for the Degree of

Doctor of Philosophy
Engineering

The University of New Mexico

Albuquerque, New Mexico

May, 2013

©2013, Pankaj Ahirwar

Dedication

This work is dedicated to my mother, Sushila and my father, Jai Ram.

Acknowledgments

I would like to thank my advisor, Prof. Ganesh Balakrishnan for his support and motivation. I am always amazed by the way he thinks and his approach towards solving a problem.

I would also like to thank my committee members, Prof. Kevin J. Malloy, Prof. Sanjay Krishna, and Prof. Thomas J. Rotter.

Special Thanks to Prof. Thomas Rotter (Tom) who not only taught me the art and science of MBE growth but also lot of other characterization techniques such as PL, X-rays diffraction, AFM, Hall-measurements etc. I would like to thank Chris Hains for his guidance in several fields, valuable inputs during manuscript preparation and preparation of final defense presentation. Many thanks to Darryl Shima for doing XTEM and SEM analysis of VECSEL samples. I would also like to thank my collaborators at University of Arizona (Prof. Moloney's Group)

I would also like to thank Shilpa, Inian, Tom, Manoj Kr., Pearlson, Rakesh Mahto, Nish, Mehak, Rishi, Anushka and all friends in Albuquerque, India and elsewhere. My colleagues and officemates of Rm. 117 (Stephen Clark [Senior UG & Lab-ninja], Myers, Brianna, John, Ted, Orlando, Emma and Sadhvikas).

In the end, I would like to thank my brothers Kapil & Mahendra, my sister Archana and my cute nieces Aani (Anveshi) & Paani (Manvika).

Design, Growth and Optimization of 2-μm InGaSb/AlGaSb quantum well based VECSELs on GaAs/AlGaAs DBRs.

by

Pankaj Ahirwar

B. Tech. (Electrical Engineering), Indian Institute of Technology, Roorkee, India, 2005

PhD, Engineering, University of New Mexico, 2013

Abstract

The antimonide based vertical external cavity surface emitting lasers (VECSELs) operating in the 1.8 to 2.8 μm wavelength range are typically based on InGaSb/AlGaSb quantum wells on AlAsSb/GaSb distributed Bragg reflectors (DBRs), grown lattice-matched on GaSb substrates. In this work the ability to grow such antimonide VECSEL structures on GaAs substrates is explored. The growth of such III-Sb VECSELs on GaAs substrates is non-trivial due to the 7.78% lattice mismatch between the antimonide based active region and the GaAs/AlGaAs DBR. The challenge is therefore to reduce the threading dislocation density in the active region without a very thick metamorphic buffer and this is achieved by inducing 90° interfacial misfit dislocation arrays between the GaSb and GaAs layers. In this work cross section transmission electron microscopy is used to analyze a variety of approaches to designing and growing III-Sb VECSELs on GaAs substrates to achieve a low threading dislocation density. The failure mechanisms in such growths and the extent to which

the threading dislocations permeate a thick active region are also analyzed. Finally, growth strategies and techniques to enable low-defect density III-Sb VECSEL active regions on GaAs are discussed.

Contents

List of Figures xii

List of Tables xix

Glossary xx

1 Introduction 1

1.1 Need for Semiconductor lasers operating $\sim 2\ \mu$m wavelength 3

1.2 Status of 2 μm laser technology 3

1.3 VECSELs operating at 2 μm. 4

1.4 Motivation and organization of the dissertation 6

References 8

2 VECSEL: Device Physics and Design 11

2.1 Principles of LASER Operation. 12

2.1.1 Basic LASER operation. 12

2.1.2 Semiconductor laser 14

2.2 Vertical-external-cavity surface emitting laser 15

2.2.1 VECSEL: Structure Design 17

2.2.2 External Cavity: Geometry and Design 19

2.2.3 DBR design 20

2.2.4 Gain Region 22

2.2.5 Subcavity design 24

2.3 Thermal Management 27

2.3.1 Need for Thermal Management in VECSELs 27

2.3.2 Strategies for Thermal Management in VECSELs 27

2.4 2 μm VECSEL Devices 30

2.4.1 Choosing the III-Sb alloys for $\sim 2\mu$m operation 30

2.4.2 2 μm gain region 31

2.4.3 Fabrication issues with III-Sb mirrors and thermal management. 31

2.5 Need for alternate substrate for 2 μm VECSEL growth 34

References **37**

3 MBE growth and Optimization of VECSEL structures. **40**

3.1 Epitaxial Growth 40

3.1.1 Molecular Beam Epitaxy 41

3.1.2 RHEED calibrations 43
3.2 VECSEL growth and Optimization 45
3.2.1 Interfacial Misfit Dislocation Array-Based Growth of GaSb on GaAs 46
3.2.2 Optimization of IMF based Quantum Wells 52
3.2.3 Distributed Bragg Reflector: Growth and Characterization . . 57
3.2.4 VECSEL subcavity design and growth 59
3.2.5 VECSEL structure growth optimization 64

References **69**

4 VECSEL: Lasing Characterization and Performance Analysis **71**
4.1 LASER Characterization 72
4.1.1 Pulsed Lasing Characterization 72
4.1.2 CW Lasing Characterization 74
4.2 Effects of mismatched epitaxy on VECSEL performance 78
4.2.1 Rate equation based performance analysis of VECSELs 79
4.2.2 TEM based analysis of threading dislocations in VECSELs . . 83
4.2.3 Effect of Threading Dislocations on Thermal Conductivity . . 87
4.3 Strategies for Threading Dislocation reduction 90
4.3.1 Optimization of the IMF interface using time-resolved PL measurements. 90

4.3.2 Placement of III-Sb active region away from the IMF Interface. 93

References **95**

5 Conclusions and Future Directions **97**

List of Figures

1.1 Absorption lines for selected chemicals in the 1.8-3.2 μm waveband taken from the Hitran 2004 database (Figure taken from [3]) 2

1.2 Schematic of a VECSEL. 5

2.1 Photon-carrier interaction processes in semiconductors, (a) absorption, (b) spontaneous emission, and (c) stimulated emission. (Figure taken from [1]) 12

2.2 (a) Edge-emitting laser, (b) Surface-emitting laser (Figure taken from [2]) 14

2.3 Schematic illustration of a VCSEL device (Figure taken from [1]) 15

2.4 Schematic band gap diagram of an optically pumped VECSEL chip and its operating principles. The antinodes of cavity standing wave are aligned on the quantum well. (Figure taken from [2]) 17

2.5 Schematic of a linear VECSEL cavity. (Figure taken from [18]) 18

2.6 (a) Modeled reflectivity from 19 pair GaSb/AlAsSb DBR (blue-curve) (b) Modeled reflectivity from 25 pair GaAs/AlGaAs DBR (red-curve). 21

2.7 Design for a VECSEL with 9 QWs, 1 QW per field antinode. 26

2.8 Strategies for thermal management for VECSELs. 28

2.9 Band gaps and lattice constants for III-V semiconductors at room temperature. 30

2.10 Experimental and Theoretical comparison of PL for $Ga_{0.8}In_{0.2}Sb$ QW and three different barrier compositions (top) barrier: $Al_{0.25}Ga_{0.75}Sb$ (middle) barrier: $Al_{0.10}Ga_{0.90}Sb$ (bottom) barrier : $Al_{0.05}Ga_{0.95}Sb$. 32

2.11 Pyramidal defects on surface of GaSb/AlAsSb DBRs grown on different substrates (left) n-doped GaSb substrate (right) Un-doped GaSb substrate. 33

3.1 Schematic of a MBE growth chamber. (Figure taken from [1]) 41

3.2 (left) 2x4 GaAs RHEED pattern (right) Estimating GaAs growth rate using damped sine fit 43

3.3 Arrhenius plot of GaAs RHEED oscillations. 44

3.4 (a) Growth of first-few monolayers of GaSb on GaAs (90° misfit dislocations underneath the GaSb islands, (b) Coalescence of islands lead to 60° misfit dislocation which can act as source of threading dislocations, (c) GaSb epi-layer grown with non-coherent coalescence of islands, (d) Cross-sectional TEM image of 100% relaxed GaSb island on GaAs, (e) Sb (2x8) reconstruction on GaAs, (f) Completely relaxed islands of GaSb on GaAs, also shown are coherently linked misfit dislocations underneath these islands, (g) GaSb epi-layer formed as a result of coherently linked misfit dislocations underneath GaSb islands. (Figure taken from [11]) . . 47

3.5 HR-TEM Image of GaSb epi-layer on GaAs. Also shown is failure point of the interface and 60° threading dislocations originating from failure point. (Figure taken from [11]) 49

3.6 (a) Atomic force micrograph of GaSb on GaAs with an optimized IMF array at the GaSb/GaAs interface. (b) cross-section TEM image of GaSb grown on GaAs with a periodic IMF array at the interface. (Figure taken from [12]) 50

3.7 XRD (004) scan of a 0.5 μm GaSb on GaAs substrate grown using IMF and non-IMF growth mode. (Figure taken from [5]) 51

3.8 PL of a structure with 11 nm thick $Ga_{0.75}In_{0.25}Sb$ quantum wells, grown on a GaAs substrate (blue), and grown on a GaSb (red). For comparison a simulated PL spectrum for $Ga_{0.75}In_{0.25}Sb$ quantum wells is included (black). (Figure taken from [12]) 53

3.9 PL of several structures as in Table 3.1 with quantum wells of varying thickness and In content. For a $Ga_{0.75}In_{0.25}Sb$ well the emission wavelength can be tuned to 2 μm by increasing the well thickness to 12 nm, but the intensity drops significantly compared to a 10 nm thick well. Higher PL intensity near 2 μm wavelength can be achieved with a 10nm thick quantum well with 28% In content. 54

3.10 PL of a structure with 10 nm thick $Ga_{0.72}In_{0.28}Sb$ quantum wells, grown at 475 °C (a), and at near 490 °C (b). For comparison the emission wavelength of b can also be achieved by a structure with 12 nm thick $Ga_{0.72}In_{0.28}Sb$, grown at 475°C (c). (Figure taken from [12]) 55

3.11 Influence of the Sb flux, measured as beam equivalent pressure (BEP) on the PL of a VECSEL active region with 9 quantum wells (grown on GaAs). (Figure taken from [12]) 56

3.12 left: AFM (5 μm x 5 μm) of GaAs/AlGaAs DBRs with surface roughness $\sim$ 0.3 nm (r.m.s.), right: Nomarski image showing extremely low surface defect density for optimal optical pumping. 57

3.13 Nomarsky image showing crosshatching of surface when AlAsSb epi-layer is not lattice matched to GaSb substrate. 58

3.14 (004) X-rays diffraction scan for AlAsSb layers for various As-valve openings. While keeping Sb-flux constant As-flux is increased for each growth to achieve lattice-matching with GaSb substrate. 59

3.15 (left) Surface nomarsky image of a lattice-matched AlAsSb epilayer (004) X-rays diffraction scan for LM-AlAsSb layer, AlAsSb epi-peak is within $\sim$ 50 arcseconds of the GaSb substrate peak. 60

3.16 L8-23 and L8-45 are active regions with 4 QWs, grown with different growth temperature management which accounts for the wavelength shift. For comparison L7-365 is a similar test structure where the 4 QWs are separated by only 20 nm of $Al_{0.3}Ga_{0.7}Sb$ as in Table 3.1. L8-46 is similar to L8-45, but has 9 QWs. 61

3.17 X-rays diffraction (XRD) spectra of VECSEL active regions grown on GaAs and grown on the AlGaAs/GaAs DBR. The right most sharp peaks (at 0 arcsec) are the GaAs substrate peaks of both structures. R8-122 (red) shows next to it (at about -400 arcsec) the peak originating from the $Al_{0.95}Ga_{0.05}As$ layers of the DBR. The peaks between -900 and -1100 arcsec indicate the active region's GaSb, AlSb and AlGaSb layers, whereas the wide peaks between -1200 and -1400 arcsec indicate the quantum wells. The angular shift of the III-Sb-peaks between the black and the red curve (active region grown on GaAs and grown on the DBR, respectively) is due to the different surface orientation of the DBR (2° off from (001) toward (011)) compared to the GaAs wafer (001) on which R8-115 was grown. . 62

3.18 Optical field (normalized E^2) and refractive index n inside the VECSEL subcavity. This outlines the difference of the subcavity designs (1) above and (2) below. 63

3.19 (a) Schematic of LMM-VECSEL (b) Schematic of LM-VECSEL (Figure taken from [11]) 64

3.20 Edge PL spectra from a VECSEL sample. (Figure taken from [12]) . . . 65

3.21 Surface PL spectra from a VECSEL sample. (Figure taken from [12]) . . 66

3.22 Temperature dependent reflectivity (TDR) spectra from a III-Sb VECSEL grown on GaAs/AlGaAs DBR. (Figure taken from [12]) 67

3.23 Temperature dependent reflectivity spectra from a VECSEL with growth rates not well calibrated, the gain-peak is much shorter than micro cavity resonance-peak 68

4.1 Schematic for optically pumped VECSEL operated in pulsed mode. (Figure taken from [1]) 72

4.2 Peak output-power Vs peak pump power for the pulsed III-Sb VECSEL on GaAs substrate. (Figure taken from [1]) 73

4.3 Time resolved pump and 2μm VECSEL pulse shapes. (Figure taken from [2]) 74

4.4 Schematic for optically pumped VECSEL operated in CW mode.(Figure taken from [1]) 75

4.5 Comparison of the two VECSELs R8-130 and R8-122 operated with a SiC heat spreader and an output coupler with 99% reflectance at -5 °C. . . . 76

4.6 Output power versus absorbed pump power of the VECSEL R8-130 operated with a SiC heat spreader and an output coupler with 99% reflectance at different operating temperatures. The maximum output power achieved is 120 mW CW at 130 μm pump spot diameter. The maximum temperature for CW operation in this arrangement is 20°C, the pump threshold at this temperature is 13.9 kW cm^{-2}. (Figure taken from [1]) 77

4.7 Output power versus absorbed pump power of the LM-VECSEL operated with a diamond heat spreader and an output coupler with 96% reflectance. The maximum output power achieved is 2.95W CW at 400 μm pump spot diameter. (Figure taken from [1]) 78

4.8 Schematic representation of carrier recombination processes in semiconductor lasers (a) Recombination via defect states (b) Spontaneous recombination processes (c) Auger recombination processes (d) carier non-capture and escape processes (Figure taken from [4]) 80

4.9 Internal quantum efficiency versus incident pump power density. Black circles: experimental η_i for LM-VECSEL. Gray-circles: Experimental η_i for LMM-VECSEL. Black-line: theory assuming a defect recombination coefficient A^{-1}= 16ns. Gray-line: theory assuming a defect recombination coefficient A^{-1}= 2.6ns. (Figure taken from [5]) 83

4.10 TEM comparison of LMM-VECSEL and LM-VECSEL. (a) shows the lattice mismatched structure with extensive threading dislocations in the active region and (b) shows the complete absence of threading dislocations in the lattice matched structure. (Figure taken from [1]) 84

4.11 (a) STEM image of LMM III-Sb VECSEL on GaAs/AlGaAs DBR showing the source of the threading dislocations at the IMF array (b) subsequent reduction in the density as a function of distance from the mismatched interface. (Figure taken from [1]) 86

4.12 (a) Schematic of III-Sb PL Test sample grown epitaxially on GaAs with IMF (b) Schematic of III-Sb PL Test sample grown epitaxially on GaAs without IMF. 91

4.13 STEM image of GaSb/AlAsSb DBR on GaAs substrate (subsequent reduction in the threading dislocation density away from the mismatched interface can be seen). (Figure taken from [17]) 94

List of Tables

1.1 Various Lasers operating $\sim 2\mu$m 4

2.1 Design Parameters for GaAs/AlGaAs DBR and GaSb/AlAsSb DBRs at a design wavelength = 2μm. 21

2.2 Thermal Conductivities at 300K for typically used DBR layers. . . . 29

3.1 Basic structure of III-Sb based quantum well active regions for PL studies, grown on a GaAs substrate using the IMF. 52

4.1 Key lasing performance metrics for a lattice-mismatched III-Sb VECSEL on GaAs/AlGaAs DBR versus those for a lattice-matched VECSEL grown on GaSb/AlAsSb DBR. 79

4.2 Experimental Fitting Data results for determining ground-state decay time constant. 93

Glossary

a.u.	Arbitrary units.
DBR	Distributed Bragg Refector.
VCSEL	Vertical cavity surface emitting laser.
VECSEL	Vertical external cavity surface emitting laser.
LM-VECSEL	III-Sb VECSEL grown on a GaSb substrate.
QW	Quantum well.
LMM-VECSEL	III-Sb VECSEL grown on a GaAs substrate.
TDD	Threading Dislocation Density.
RHEED	Reflection High Energy Electron Diffraction.
CW	Continuos Wave.
MBE	Molecular Beam Epitaxy.
TDR	Temperature Dependent Reflectivity.
PL	Photoluminescence.

Chapter 1

Introduction

The first LASER (Light Amplification by Stimulated Emission of Radiation) was made in 1960 and since its invention and demonstration, several types of lasers have been developed, for example semiconductor-laser, solid-state laser, gas-laser, dye-laser and excimer-laser[1, 2]. Lasers are used in wide variety of applications, optical communication, material processing, laser-welding, imaging, entertainment etc. The most important properties of lasers which enable their use in several fields are;

- laser-emission wavelength tunability (from UV to MID-IR)
- output optical power scalability (few mW to several kW)
- method of excitation (optical pumping or electrical carrier injection)
- output beam quality
- device-size and integration in other subsystems
- high-speed modulation and short-pulse generation ability

Each type of lasers discussed above have advantages and disadvantages. The applications of a particular class of laser depends on whether advantages outweigh disadvantages for that particular application.

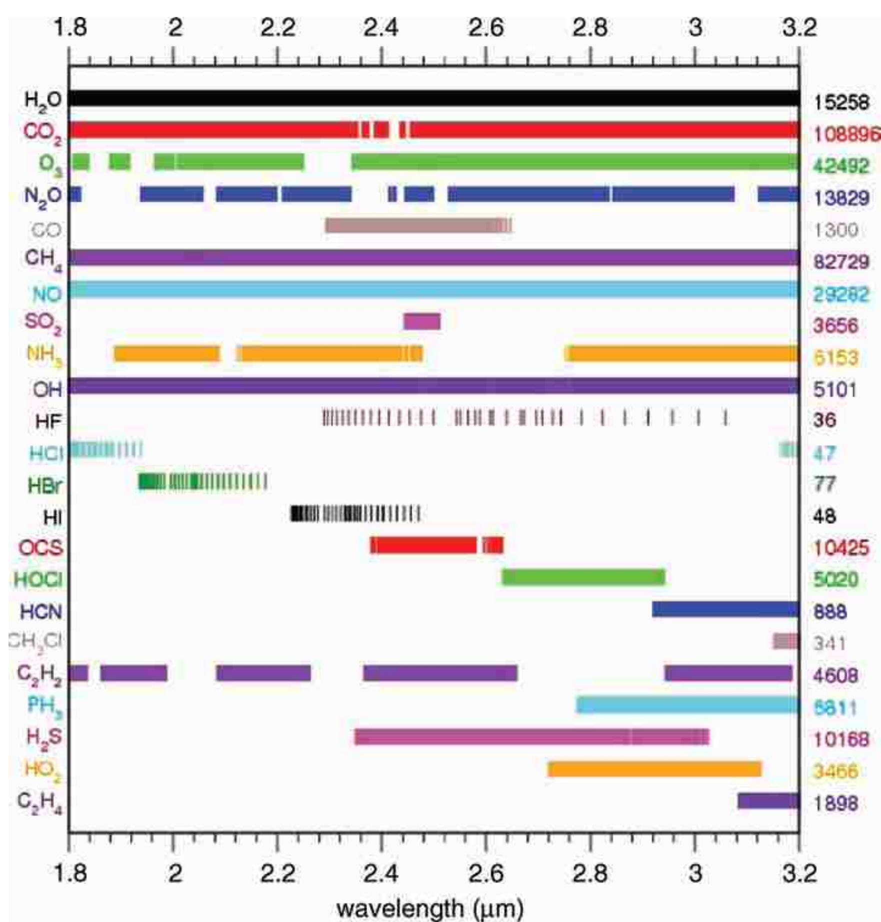

Figure 1.1: Absorption lines for selected chemicals in the 1.8-3.2 μm waveband taken from the Hitran 2004 database (Figure taken from [3])

1.1 Need for Semiconductor lasers operating ~ 2 μm wavelength

The 1.8-2.0 μm wavelength range is of special interest, as several air pollutant molecules show fundamental absorption [4] in this wavelength range. Measurement of trace gas concentrations can thus be performed using laser absorption spectroscopy. Figure 1.1 shows the absorption spectra of important atmospheric gases. Some of the gases shown in this spectra are atmospheric pollutants (CH_4, SO_2, CO etc.) The detection of these industrial pollutants can benefit significantly by availability of efficient, high-power and high-beam quality light sources. The solid-state lasers [5, 6] and fiber lasers [7] can emit several hundreds of watts of output power and have excellent beam quality, but their emission wavelengths are restricted to discrete electronic transitions. Semiconductor lasers on the other hand can be easily designed to cover this range of wavelength (1.8-2.0 μm). In electrically injected configuration they can be made very compact and integrated directly with electronic circuits. In optically injected configuration semiconductor lasers can demonstrate high-output powers. The beam quality depends on how laser emission is coupled out of a semiconductor laser cavity. Thus not only gas detection but several other applications such as infrared countermeasures, LIDAR etc. can benefit from high-power, high-beam quality semiconductor lasers operating near 2 μm wavelength.

1.2 Status of 2 μm laser technology

Table 1.1 lists the various kind of lasers operating at $\sim 2\mu$m wavelength. The type of active region or gain-medium is also listed for each laser type. Vertical external-cavity surface-emitting lasers (VECSELs) have significant attributes such as compact size, good beam quality, high efficiency, high-output power and emission wavelength

tunability which allow them to be used in several areas[8, 9, 10]. The physics, structure design and operation principles of VECSELs are discussed in detail in Chapter 2.

Table 1.1: Various Lasers operating $\sim 2\mu$m .

Description	Type	Reference
III-V InGaAsP based lasers	Semiconductor diode Laser	[13, 11]
III-V InGaAsSb based lasers	Semiconductor diode Laser	[14, 1, 12]
InAs Q-Dash based Lasers	Semiconductor diode Laser	[15]
Tm:YAG	Solid state Laser	[16]
Tm-Fiber Laser	Fiber Laser	[17]
III-Sb VECSEL	VECSEL	[18, 1]

1.3 VECSELs operating at 2 μm.

A schematic of VECSEL is shown in Figure 1.2. A VECSEL has several distinct advantages over other types of lasers;

- optical pumping allows uniform pumping in a large area where the carriers are automatically confined by the pump spot
- no p-n junctions and contacts thus simpler processing and growth steps
- ability to scale output power with pump-spot size (given pump intensity and cavity configuration is kept same)
- nearly circular TEM_{00} beam at multi-watt power output
- external-cavity allows introduction of external elements in cavity

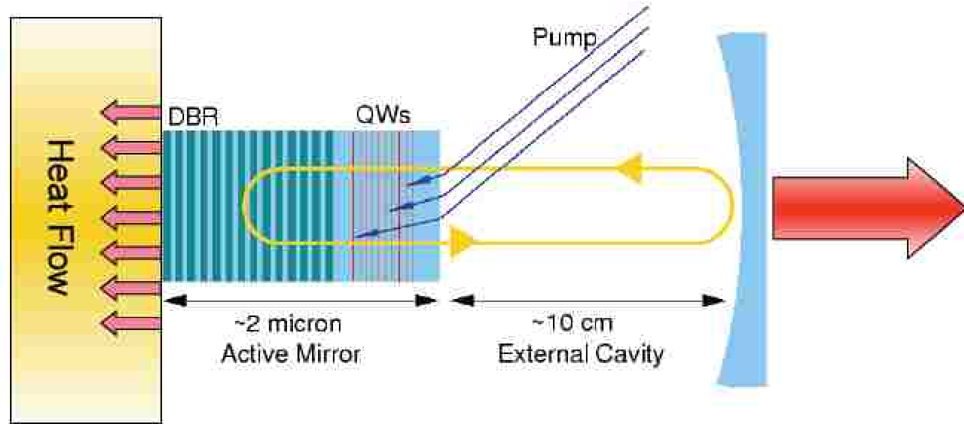

Figure 1.2: Schematic of a VECSEL.

The majority of VECSELs operating at or near 2μm wavelength range are typically based on InGaAsSb/AlGaAsSb quantum wells on AlAsSb/GaSb distributed Bragg reflectors (DBRs) grown lattice-matched on GaSb substrates[19, 20]. The maximum power obtained from a single antimonide VECSEL chip is still less than 10 Watts CW. However the arsenide VECSELs based on InGaAs quantum wells (grown epitaxially on GaAs substrates) have already broken the 100 Watts (CW Output power) barrier from a single chip[21]. The main reason for the order of magnitude reduction in the maximum CW power achieved by VECSELs on GaAs versus the GaSb based lasers can be primarily attributed to thermal management issues[22, 23]. One of the primary reason for thermal bottleneck in III-Sb based VECSELs is poor thermal conductivity of the GaSb substrate. Also the lack of good etch-stop layers and etch chemsitry for III-Sb material system prevent complete removal of the GaSb substrate from III-Sb VECSEL devices. The problem of scaling available output power from III-Sb VECSELs can be solved by growing the III-Sb VECSELs on GaAs substrates (which have much better substrate removal techniques).

1.4 Motivation and organization of the dissertation

In this body of research the ability to grow GaSb based active regions directly on GaAs substrates by inducing an interfacial array of misfit dislocations (IMF) is explored. The study further investigates the ability to grow such active regions on GaAs/AlGaAs DBR to investigate the effects of the highly mismatched interface on the performance of the VECSEL.

Chapter 2 is devoted to the fundamental design aspects of VECSELs, and in particular VECSELs operating in the MID-IR wavelength. Section 2.2 deals with general operating principles of VECSEL, whereas Section 2.4 focuses on various design aspects of antimonide-based VECSELs for operation at or close to 2μm.

Chapter 3 is about epitaxial growth and characterization of the VECSEL structures. Section 3.1 introduces the concepts of MBE growth and section 3.1.2 talks about calibration of group-III sources using RHEED calibrations. The rest of the chapter is devoted to various experiments related specifically about epitaxial growth of GaSb on GaAs substrates, optimization of III-Sb active regions grown on GaAs (Section 3.2.2), DBR epitaxial growth and characterization (Section 3.2.3) and finally VECSEL epitaxial growth and optimizations of the VECSEL structures (Sections 3.2.4, 3.2.5).

Chapter 4 discusses lasing characterization of the grown VECSEL devices. Pulsed and CW lasing performance are compared for the different VECSEL designs. Furthermore the chapter discusses the TEM and rate equation based performance analysis of the lattice-matched and lattice-mismatched VECSEL samples. The chapter also discusses the techniques for better growth of IMF based VECSEL samples and ways to reduce threading dislocations in active region of lattice-mismatched VECSEL

devices.

Chapter 5 discusses conclusions and future directions.

References

[1] O.G. Okhotnikov, *Semiconductor Disk Lasers:Physics and Technology*, Weinheim, Germany: Wiley-VCH Verlag GmbH & Co. KGaA, Apr. 2010.

[2] Coldren, L.A. and Corzine, S.W., *Diode Lasers and Photonic Integrated Circuits*, John Wiley & Sons, Inc., New York, 1995.

[3] Garnache, A., Kachanov, A.A., Stoeckel, F., and Planel, R., *Highsensitivity intracavity laser absorption spectroscopy with VECSELs*, Opt. Lett., 24, 826828, 1999.

[4] Holm, M.A., Burns, D., Ferguson, A.I., and Dawson, M.D., *Actively stabilized single-frequency VECSEL AlGaAs laser. IEEE Photon. Technol. Lett.*, 11, 15511553, 1999.

[5] Koechner, W., *Solid-State Laser Engineering*, 6th edn, Springer, 2006.

[6] Koechner, W. and Bass, M., *Solid-State Lasers: A Graduate Text*, Springer, 2003.

[7] Digonnet, M.J.F. (ed.), *Rare- Earth-Doped Fiber Lasers and Amplifiers*, 2nd edn, CRC Press, 2001.

[8] Triki, M., Cermak, P., Cerutti, L., Garnache, A., and Romanini, D., *Extended continuous tuning of a single frequency diode-pumped vertical external- cavity surface-emitting laser at 2.3 μm.* Photonics Technology Letters, IEEE, 20, 19471949, 2008.

[9] M. Kuznetsov, F. Hakimi, R. Sprague, and A. Mooradian, *High-power ($>$ 0.5-W CW) diode-pumped vertical-external-cavity surface-emitting semiconductor lasers with circular TEM_{00} beams*, Photonics Technology Letters, IEEE, 9(8):10631065, Aug. 1997.

[10] Li, H. and Iga, K. *Vertical- Cavity Surface-Emitting Laser Devices*, Springer, 2002.

[11] Kapon, E. *Semiconductor Lasers I: Fundamentals*, Academic Press, 1999.

[12] Kapon, E. *Semiconductor Lasers II: Materials and Structures*, Academic Press, 1999.

[13] Major, J.S., Nam, D.W., Osinski, J.S., Welch, D.F., *High-power 2.0 μm InGaAsP laser diodes*, Photonics Technology Letters, IEEE , vol.5, no.6, pp.594,596, June 1993.

[14] Diehl, R. High Power Diode Lasers, Springer, 2000.

[15] Thomas. J. Rotter, *Growth and properties of self assembled InAs quantum dash laser active regions*, Dept. Phy. Astron., Univ. New Mexico, Albuquerque, 2007.

[16] T. Back et al. *Thulium:YAG 2 micron CW laser prostatectomy : where do we stand*, World J Urol. 28,163-168, 2010.

[17] Shibin Jiang, *Recent progress on 2-micron fiber lasers*, Optical Fiber Communication Conference and Exposition (OFC/NFOEC), 2011 and the National Fiber Optic Engineers Conference , vol., no., pp.1,3, 6-10 March 2011.

[18] J.M. Hopkins, N. Hempler, D. Burns, N. Schulz, B. Rsener, M. Rattunde, C. Manz, K. Khler and J. Wagner, *High-power, GaSb-based Semiconductor disk laser at 2.0 μm*, Optics Lett. 33, 201, 2008.

[19] B. Rsener ; N. Schulz ; M. Rattunde ; C. Manz ; K. Khler, et al. *GaSb-based VECSEL exhibiting multiple-watt output power and high beam quality at a lasing wavelength of 2.25 μm*, Proc. SPIE 6997, Semiconductor Lasers and Laser Dynamics III, 699702, April, 2008).

[20] Rosener, B.; Schulz, N.; Rattunde, M.; Manz, C.; Kohler, K.; Wagner, J., *High-Power High-Brightness Operation of a 2.25 μm (AlGaIn)(AsSb)-Based Barrier-Pumped Vertical-External-Cavity Surface-Emitting Laser*, Photonics Technology Letters, IEEE , vol.20, no.7, pp.502,504, April, 2008.

[21] B. Heinen, T. L. Wang, M. Sparenberg, A. Weber, B. Kunert, J. Hader, S.W. Koch, J.V. Moloney, M. Koch, W. Stolz, *106 W continuous-wave output power from vertical-external-cavity surface-emitting laser*, Electron. Lett.,vol. 48, no. 9, pp. 516-517, Apr. 2012.

[22] Giet, S., Kemp, A. J., Calvez, D. B. S., Dawson, M. D., Suomalainen, S., Harkonen, A., Guina, M., Okhotnikov, O., and Pessa, M., *Comparison of thermal management techniques for semiconductor disk lasers*, in [Technology and Devices], Solid State Lasers XVIII , (2008).

[23] Tropper, A. C. and Hoogland, S., *Extended cavity surface-emitting semiconductor lasers*, Prog. Quantum Electron. 30, 1-43 (2006).

Chapter 2

VECSEL: Device Physics and Design

In this chapter the basic operating principles and design of the building blocks of VECSEL are discussed. A VECSEL is a semiconductor laser typically consisting of an integrated high reflectivity mirror, a gain-region and a partially transmitting external spherical dielectric mirror (also known as an output coupler). Similar to other semiconductor devices, the optoelectronic properties of VECSELs, such as absorption and gain can significantly vary with wavelength, carrier density, temperature etc. In this section I will discuss the physics of VECSELs to better understand the device modeling and their operation.

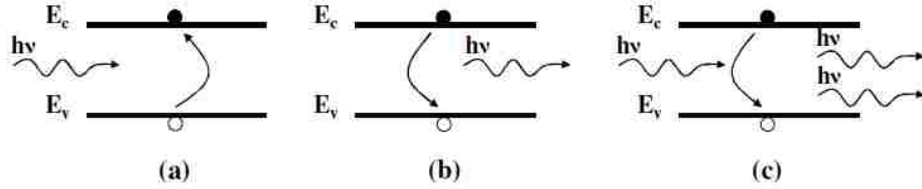

Figure 2.1: Photon-carrier interaction processes in semiconductors, (a) absorption, (b) spontaneous emission, and (c) stimulated emission. (Figure taken from [1])

2.1 Principles of LASER Operation.

2.1.1 Basic LASER operation.

A Laser is comprised of a gain medium capable of emitting photons at a given wavelength. This photon-emitting medium is called an active or gain region. The gain medium can be a gas or a solid (semiconductor or crystal). In the simplest configuration the gain medium is positioned between two reflecting mirrors which form an optical cavity. One of the mirrors forming the optical cavity is highly reflecting and the other is a partially reflecting mirror. Electrons in the active region are excited to higher energy levels by an external pump source, and then relax back to their original state emitting a photon. Figure 2.1(a) shows optical excitation by another photon (optical pumping), exciting an electron from lower energy level to higher energy level. When an electron makes transition from higher energy level to a lower energy level, the energy difference can be emitted in form of a photon. (Figure 2.1(b)) This photon may simulate other electrons to make transition from higher energy levels to lower energy levels, producing more photons that can simulate even more elections to make the transition. This phenomenon is known as stimulated emission. (Figure 2.1(c)) The photons created in this process have same phase, wavelength and direction as the photon which stimulated the emission.

The photons generated in the active region traverse back and forth in the cavity. At the partially reflecting mirror at one end of the cavity, some photons are reflected back and some are transmitted. The photons circulating in the cavity simulate other electrons to make transition from higher energy level, to lower energy levels. The concentration of electrons in higher energy level should be higher than concentration of electrons in lower energy level. This is known as population inversion. This population inversion is maintained by external pumping (optical or electrical). The energy of the emitted photons is related to energy difference between two electron energy levels;

$$\lambda = \frac{hc}{(E_2 - E_1)}\,, \tag{2.1}$$

For operation of a laser, the gain per unit length should overcome total losses (per unit length) in laser structure. If 'g' is the gain per unit length and α_i is the internal loss per unit length, then net power gain 'G' after one round trip is: $G = exp(2(g - \alpha_i)L)$, here L is the length of gain medium. The condition for lasing is that the roundtrip gain should exceed 1. Taking into account the losses from the mirrors the condition for lasing becomes; $R_1R_2(G)^2 \geq 1$

$$R_1R_2e^{2(g-\alpha_i)L} \geq 1\,, \tag{2.2}$$

$$g \geq \alpha_i + \frac{1}{2L}ln\frac{1}{R_1R_2}\,, \tag{2.3}$$

The effective overlap between gain-medium and electric-field is known as confinement factor ($\Gamma = V_g/V_p$). It is simply a ratio of active region volume occupied by gain, V_g, over the cavity volume occupied by photons, V_p. The lasing threshold condition is thus given by;

$$\Gamma g_{th} = \alpha_i + \frac{1}{2L}ln\frac{1}{R_1R_2} = \alpha_i + \alpha_m\,, \tag{2.4}$$

here α_m is mirror loss prorated over the length of the cavity from both mirrors.

2.1.2 Semiconductor laser

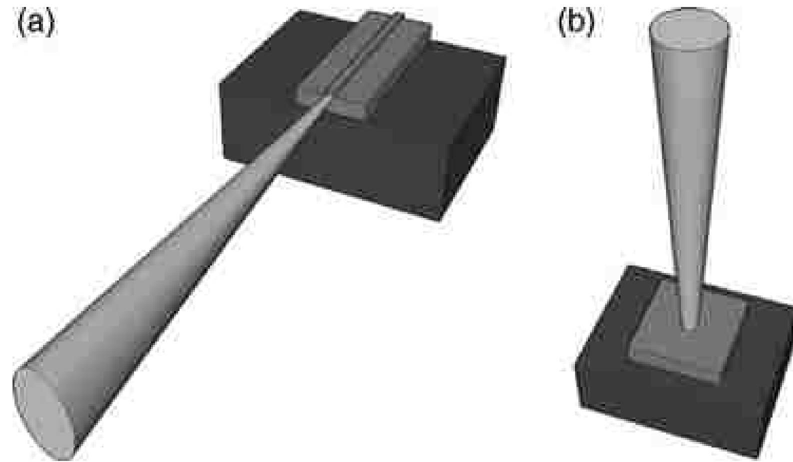

Figure 2.2: (a) Edge-emitting laser, (b) Surface-emitting laser (Figure taken from [2])

In a semiconductor laser the electrons are distributed in energy bands rather than discrete energy levels. Typically the bottom of conduction band is the high-energy level and the top of valence band is the low energy level. An electron excited from valence band leaves behind a hole in valence band. The electron and hole can combine through several mechanisms (radiative, defect assisted or Auger recombination). Electrons and holes which combine through radiative recombination emit a photon with energy equivalent to band gap difference (E_C-E_V). The photon emitting semiconductor region can either be bulk semiconductor, quantum wells, quantum dots or quantum dashes. [2] Semiconductors lasers can be grouped based on how carriers are injected in the active region (optically vs electrically injected). Based on how light emits from a semiconductor laser it can be classified into two major configurations: edge-emitting [3] and surface-emitting [4]. In case of an edge-emitting laser (Figure 2.2(a)) the light is confined in the plane of the semiconductor chip and is emitted from the edge of the chip, generally using cleaved facets as mirrors, whereas in case of surface-emitting the emission of light is in a plane perpendicular to the semicon-

ductor chip (Figure 2.2(b)). Obtaining lasers with both high optical power and a good beam quality simultaneously is a difficult task. For edge-emitting semiconductor lasers a near TEM_{00} mode is only possible for output power levels below 1W. [11, 12] Figure 2.3 shows schematic illustration of a VCSEL device. It consists of top and bottom Distributed Bragg reflectors (DBRs) formed by alternatively stacking layers of materials with different refractive indices. These can offer very high reflectivities, above 99.9%. The DBRs can be doped for electrical injection of carriers into the active-region. The light propagates in a direction along the normal to the epitaxial layers and exits from the top DBR which has lower reflectivity ($\sim$ 96-99 %). Unlike edge-emitting lasers, VCSELs have nearly circular TEM_{00} output mode, but the output power from such devices is limited to 10's of mW due to their limited lateral dimension[14].

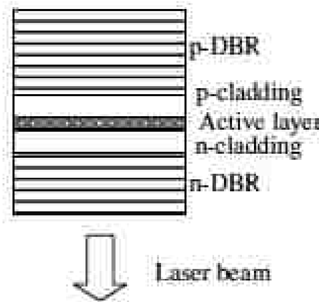

Figure 2.3: Schematic illustration of a VCSEL device (Figure taken from [1])

2.2 Vertical-external-cavity surface emitting laser

By replacing the top DBR of a VCSEL with an external concave mirror, a vertical-external-cavity surface emitting laser (VECSEL) is created[10]. For a VECSEL the lateral mode size is controlled by radius of curvature of the external mirror and it's distance from the surface of semiconductor chip. Thus high output power and nearly

circular (TEM_{00}) beam output are possible from VECSELs by adjusting the cavity dimensions for a large beam waist and matching the optical pump spot size. The power scaling in a VECSEL is achieved by increasing the diameter of the pump spot while keeping the pump density constant. For optically pumped operation of VECSEL, the incident pump photons with higher photon energy ($E_{pump}=hc/\lambda_{pump}$) are absorbed in pump-absorbing region that serves as quantum well barrier as well. The carriers then diffuse to the smaller band gap energy region (quantum wells), which emit photons with lower photon energy ($E_{QW}=hc/\lambda_{QW}$). The pump absorption and laser gain properties can be optimized independently due to separate absorption layers (barriers) and quantum well emission layers. A higher bandgap layer (clad or window layer) is typically placed at both ends of absorption region for better carrier-confinement. The window layer near the chip surface prevents carriers from diffusing to the air-semiconductor interface. Carriers can combine non-radiatively near the surface and can thereby reduce laser gain.

The operating temperature of the VECSEL plays an important role in determining device performance. The pump laser photon energy difference, together in combination with other laser inefficiencies is dissipated as heat in the active region of the device. This energy, if not dissipated efficiently from the active region can increase the temperature of the active region. With increased temperature in the active region, excited carriers have a higher chance of recombining non-radiatively and escaping thermally from the quantum well to the barrier regions depleting the laser gain and turning the laser off in a thermal rollover process [11]. Such thermal rollover is the dominant mechanism which limits the high power operation of VECSELs. The quantum well gain is dependent on temperature since both the band gap and Fermi-Dirac carrier distributions are functions of temperature. The micro cavity resonance and quantum well gain red-shift with respect to temperature and typically the gain peak shift is faster when compared to that of the micro cavity. A gain offset detuning between the QW's gain peak and the microcavity resonance is therefore commonly

implemented as a strategy to mitigate the effect of different red-shift rates. Optical pumping is the most straightforward way to obtain uniform pumping in large area, making the power scaling of VECSELs much simpler. Optical pumping also defines the gain region and lateral carrier confinement region. Inside the pump-spot region, the cavity mode experiences gain and experiences loss elsewhere.

2.2.1 VECSEL: Structure Design

Figure 2.4 shows the bandgap diagram of a semiconductor VECSEL, and explains the functions of various layers and also illustrates the laser operating principle.

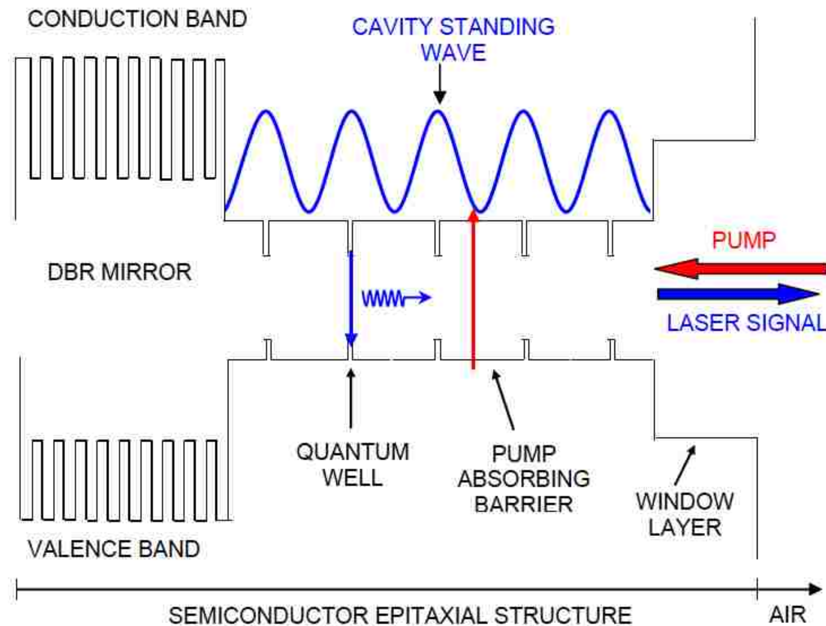

Figure 2.4: Schematic band gap diagram of an optically pumped VECSEL chip and its operating principles. The antinodes of cavity standing wave are aligned on the quantum well. (Figure taken from [2])

A VECSEL semiconductor structure is comprised of following subsections: a DBR

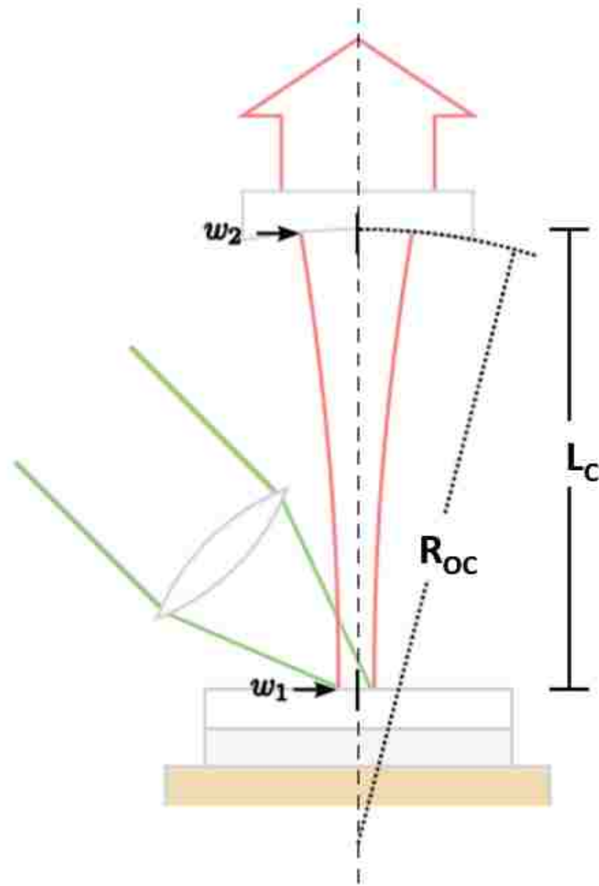

Figure 2.5: Schematic of a linear VECSEL cavity. (Figure taken from [18])

mirror, a gain section (with quantum wells and barriers) and carrier confinement regions and a cap layer to protect layers underneath from oxidation. The gain section commonly uses quantum wells as active region although quantum dots, quantum dashes and bulk semiconductors can also be used. The semiconductor structure along with an external mirror forms the laser cavity. In the following sections the various components and building blocks of a VECSEL device are discussed.

2.2.2 External Cavity: Geometry and Design

The optical elements forming a VECSEL cavity are external to the laser chip except the on-chip DBR mirror. The optical cavity allows control of the fundamental transverse mode size as well as the insertion of various intracavity elements such as non-linear crystals for frequency doubling or saturable absorbers for passive mode-locking. The simplest cavity is the linear cavity discussed thus far. In this work a linear cavity is used for lasing characterizations of all VECSEL chips. Figure 2.5 shows a simple two mirror VECSEL cavity of length L_C, one of the mirrors is the on-chip DBR while the other is a curved mirror with radius of curvature; R_{OC}. The radius of curvature (R_{OC}) of the output coupler in combination with length of cavity (L_C) can be chosen so as to achieve operation in a near (TEM_{00}) mode. The transmission matrix T is obtained by multiplying propagation over distance L_C from VECSEL chip to the external mirror and propagation back to VECSEL chip:

$$T = \begin{bmatrix} 1 & L_C \\ 0 & 1 \end{bmatrix} \begin{bmatrix} 1 & 0 \\ -\frac{2}{R_{OC}} & 1 \end{bmatrix} \begin{bmatrix} 1 & L_C \\ 0 & 1 \end{bmatrix} = \begin{bmatrix} 1-\frac{2L_C}{R_{OC}} & 2L_C-\frac{2L_C^2}{R_{OC}} \\ \frac{2}{L_C} & 1-\frac{2L_C}{R_{OC}} \end{bmatrix}, \quad (2.5)$$

The T matrix can thus be expressed as;

$$T \equiv \begin{bmatrix} T_{11} & T_{12} \\ T_{21} & T_{22} \end{bmatrix}, \quad (2.6)$$

The stability condition for a cavity is $0 \leq (T_{11}+T_{22}+2)/4 \leq 1$, for a linear VECSEL cavity this yields $L_C \leq R_{OC}$.[14]

The laser mode beam diameter w_1 on the VECSEL chip and w_2 on the output coupler are given by following expressions;

$$w_1^2 = \frac{4\lambda_{laser}L_C}{\pi}\sqrt{(R_{OC}-L_C)/L_C}\,, \quad (2.7)$$

$$w_2^2 = \frac{4\lambda_{laser}R_{OC}}{\pi}\sqrt{L_C/(R_{OC}-L_C)}\,, \quad (2.8)$$

Mode diameters on VECSEL chip between 100 and 200μm can be easily achieved in this linear cavity for cavity lengths less than 25mm. The pump spot size should be matched to laser mode size on the VECSEL chip in order to achieve efficient gain aperturing for fundamental transverse (TEM_{00}) mode selection.[18]

2.2.3 DBR design

In case of an edge-emitting laser, the light propagates along the gain-medium in a cavity typically several 100 μm long. In this configuration even a single QW can provide enough gain for lasing (since Γ in the direction of propagation is $\sim$1). The vertical configuration in the VECSELs limits the amount of gain achieved in one roundtrip. The mirrors thus needed to achieve lasing typically require more than 99% reflectivity which is not possible from a single cleaved semiconductor air interface.

In most circumstances, these mirrors are distributed Bragg reflectors (DBRs), which consist of $\lambda/4$ optical thickness layers of alternating low (n_{LOW}) and high (n_{HIGH}) index of refraction materials at the design wavelength ($\lambda_{\mathrm{Bragg}} = \lambda_{\mathrm{Design}}$). The reflectance of an ideal DBR with m pairs is given by following equation[14, 15];

$$R = \left[\frac{1-(n_{LOW}/n_{HIGH})^{2m}}{1+(n_{LOW}/n_{HIGH})^{2m}})\right]^2, \tag{2.9}$$

The spectral width of high reflectivity or stop-band of the DBR is given by following expression;

$$\frac{\Delta\lambda_{DBR}}{\lambda_{Bragg}} = \frac{4}{\pi} arcsin\left(\frac{1-(n_{LOW}/n_{HIGH})}{1+(n_{LOW}/n_{HIGH})}\right), \tag{2.10}$$

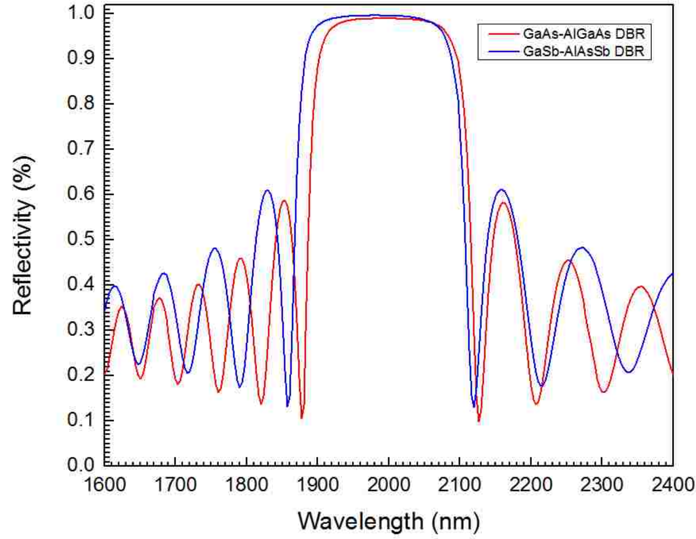

Figure 2.6: (a) Modeled reflectivity from 19 pair GaSb/AlAsSb DBR (blue-curve) (b) Modeled reflectivity from 25 pair GaAs/AlGaAs DBR (red-curve).

Figure 2.6 (red curve) shows the modeled reflectivity spectrum of the GaAs/AlGaAs DBR ($\lambda_{design} \sim 2\mu m$). It consists of 25 pairs of 149nm GaAs /172 nm $Al_{0.95}Ga_{0.05}As$. The modeled reflectivity spectrum for another DBR ($\lambda_{design} \sim 2\mu m$) is shown in Figure 2.6 (blue curve). It consists of 19 pairs of $AlAs_{0.08}Sb_{0.92}$/GaSb layers. The design parameters for the two types of DBR are shown in Table 2.1.

Table 2.1: Design Parameters for GaAs/AlGaAs DBR and GaSb/AlAsSb DBRs at a design wavelength = 2μm.

DBR	Pairs	Layers	n (at λ=2 μm)	thickness (nm)
GaAs/AlGaAs DBR	25	$Al_{0.95}Ga_{0.05}As$	2.9005	172.0
		GaAs	3.3440	149.0
GaSb/AlAsSb DBR	19	$AlAs_{0.08}Sb_{0.92}$	3.2340	153.8
		GaSb	3.7490	132.6

2.2.4 Gain Region

The light amplification in III-Sb based VECSELs originates in type I QWs embedded in a subcavity terminated by a highly reflective distributed Bragg reflector (DBR) and an interface between topmost layer and air[12, 13]. A strained type-I gain system for near 2 μm operation is based on $\mathrm{Ga}_x\mathrm{In}_{1-x}\mathrm{Sb}$ QWs and $\mathrm{Al}_x\mathrm{Ga}_{1-x}\mathrm{Sb}$ barriers. In a type I heterojunction the bands line up so that both electrons and holes are confined to the same layer.

The gain from a semiconductor quantum well has an approximately logarithmic dependance on the carrier density in the quantum well ($\mathrm{N_{QW}}$, cm^{-3});

$$g = g_0 ln(N_{QW}/N_{tr})\,, \tag{2.11}$$

where $\mathrm{N_{tr}}$ is the transparency carrier density and $\mathrm{g_0}$ is the semiconductor material gain parameter. $\mathrm{g_0}$ is an intrinsic gain of the quantum well and is given by;

$$g_0 = \frac{\pi e^2 |M|^2 |\langle F_V|F_C\rangle|^2}{\epsilon_0 m_0^2 \omega} \rho_J^{2D}\,, \tag{2.12}$$

where $|M|^2$ is squared modulus of momentum matrix element, F_V and F_C are hole and electron state envelope functions, ρ_J^{2D} is the joint density of two-dimensional electron and hole states, per unit energy, per unit cross-section of the well. For most of devices, the wells are designed such that the performance is dominated by n=1 bound states. The joint density of states therefore has the form of a single step function. Also it is independent of energy for photon energies greater than the minimum transition energy:

$$\rho_J^{2D} = \frac{m_J}{\pi \hbar^2} H(h\nu - (E_{C1} - E_{V1}))\,, \tag{2.13}$$

where H is the Heaviside function:

$$H(x) = 0, x < 0; H(x) = 1, x \geq 0\,, \tag{2.14}$$

The effective mass, m_J, represents the joint curvature of the valence and conduction bands, and is given by;

$$\frac{1}{m_J} = \frac{1}{m_e} + \frac{1}{m_h}\,, \tag{2.15}$$

where m_e and m_h are the effective masses of the electron and hole, respectively.

The VECSEL lasing threshold condition states that the intracavity optical field is reproduced in one round-trip inside the cavity;

$$R_{DBR} R_{OC} T_{loss} exp(2\Gamma_Z g_{th} N_w L_w) = 1\,, \tag{2.16}$$

where R_{DBR} and R_{OC} are the DBR and output coupler reflectivities respectively, T_{loss} is the transmission factor due to round-trip cavity loss, g_{th} is the threshold material gain, N_w is the number of quantum wells in the gain medium, and L_w is the thickness of a quantum well. Γ_Z is the longitudinal confinement factor, it characterizes overlap between the intracavity optical standing wave and the quantum wells spaced inside the active region.

The quantum wells are thin, $L_w \sim$ 8-12 nm. Due to this they provide only a small amount of gain to an optical wave propagating in a VECSEL cavity normal to plane of the quantum wells. Thus multiple wells are required for lasing. These quantum wells are placed at the antinodes of the laser optical field standing wave to provide the largest Γ_Z. More about VECSEL sub cavity design will be covered in Section 2.2.5. Strained QWs are preferred over unstrained QWs due to their better operating characteristics such as lower threshold, higher gain and improved temperature dependence[16, 5]. Since multiple QWs are used in a VECSEL structure,

one has to make sure that the total thickness does not exceed critical thickness limit. Beyond this strain relaxation occurs via crystalline defect formation and degrades laser performance because of non-radiative recombination.

2.2.5 Subcavity design

The properties of a VECSEL are determined both by the design of the gain region, and by the design of the subcavity in which they are embedded. The VECSEL subcavity is formed by DBR at one end side and the semiconductor air interface on top of the active region at other. The presence of the subcavity leads to the formation of longitudinal modes with much larger frequency spacing than the modes associated with the VECSEL cavity, because the subcavity is much shorter than the VECSEL cavity. For optimal performance, the quantum wells are placed at field antinodes of the primary modes associated with the subcavity. This is called the Resonant Peroidic Gain (RPG) arrangement[8, 9], leading to a strong coupling between quantum confined carriers and the intracavity standing wave in the active region. One or more closely spaced quantum wells can be placed near a given standing wave antinode. Typically the gain region thickness covers several periods of this standing optical field, depending on the number of quantum wells in the gain region. The benefits of a RPG design are described below. The modal gain per unit time for a VECSEL can be expressed as;

$$\langle G \rangle = \Gamma_z g_0 V^{-1} f_{CV} \,, \tag{2.17}$$

where g_0 is intrinsic gain of QW (Equation 2.12), V is the volume of the mode in air and is expressed as;

$$V = \frac{1}{2}\pi w_0^2 L_C = \frac{1}{2}\lambda L^2 \sqrt{\frac{g}{1-g}} \,, \tag{2.18}$$

The Fermi factor, f_{cv}, corresponds to the population inversion at photon energy E: $f_{CV} = f_C - f_V$, where the quantities f_C and f_V are the Fermi-Dirac occupation

numbers for the conduction and valence band states, respectively, determined by the local temperature and pumping rate.

In Eq. 2.17, the enhancement of the gain that arises from the effect of the micro-cavity, and from the position of the wells at standing-wave anti-nodes, is described by the longitudinal confinement factor Γ_z, given by

$$\Gamma_z = \frac{\sum_q |A_{i_q}^{+} exp(ik_{i_q} z_q) + A_{i_q}^{-} exp(-ik_{i_q} z_q)|^2}{|A_0^{+}|^2 + |A_0^{-}|^2}, \tag{2.19}$$

here A_i represents the transverse component of the vector potential in the ith layer in subcavity, labelled $\pm$ to denote forward or backward propagation, respectively. k_i is the propagation constant which describes the rate of change of phase along the z-axis (wave-propagation direction) in the ith layer and is given by;

$$k_i = k_0 n_i cos\left(arcsin\left(\frac{n_0}{n_i}\right)\right), \tag{2.20}$$

Here, k_0 is the propagation vector of the light in free space.

The relative longitudinal confinement factor (Γ_z) introduces a strong spectral filtering effect, influencing device performance[10]. The sharp subcavity resonance may allow VECSEL to operate at a single wavelength, if the quantum wells grown are uniform and identical and if the RPG is grown accurately.

The longitudinal confinement factor, exhibits a sharp resonance peak which is determined by the thickness of the subcavity and the reflectivity of the boundary surfaces. At the design wavelength, Γ_z reaches a peak value if all wells are precisely aligned with field anti-nodes. Thus it is very essential to accurately grow the VEC-SEL structures (accurate thickness of subcavity) with QWs positioned precisely. The MBE growth and optimizations of subcavity are discussed in detail in Chapter 3.

The position of the air-semiconductor interface with respect to the E-field pattern is a very crucial design parameter. A resonant structure (antinode of the field at the

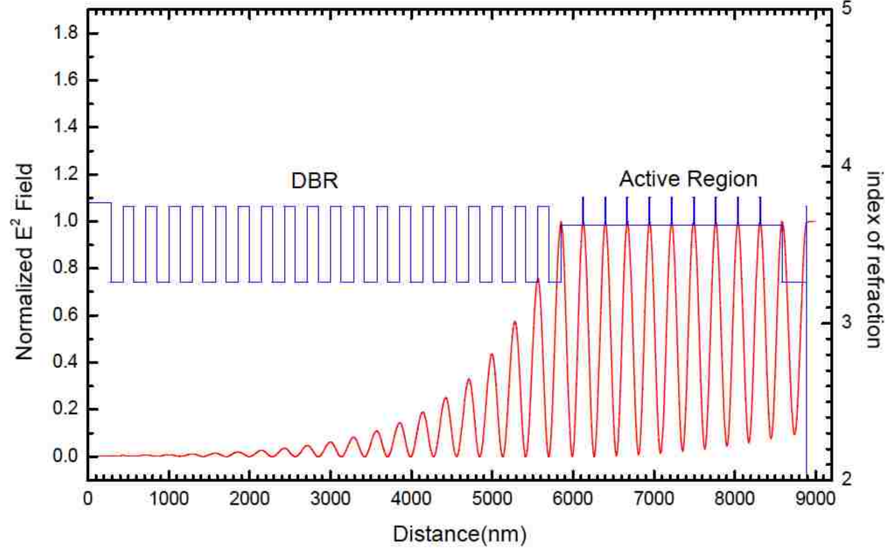

Figure 2.7: Design for a VECSEL with 9 QWs, 1 QW per field antinode.

semiconductor interface) has high effective gain, relative immunity to cavity losses, and tolerance towards added intra-cavity elements.

The effective chip gain is given by following expression;

$$G_{chip}(\lambda) = \frac{(\sqrt{R_i} - \sqrt{R_{DBR}}g_s)^2 + 4\sqrt{R_i R_{DBR}} g_s sin^2(2\pi n L_c/\lambda)}{(1 - \sqrt{R_i R_{DBR}} g_s)^2 + 4\sqrt{R_i R_{DBR}} g_s sin^2(2\pi n L_c/\lambda)}, \quad (2.21)$$

where g_s is the single-pass gain of the structure, R_{DBR} and R_i are the DBR mirror and airsemiconductor interface reflectivities, respectively, and L_c is the length of the cavity.

In this dissertation work, the subcavity design was done using Vertical[17]. Figure 2.7 shows a subcavity design with 9 QW, each QW is placed at E-field antinode and anti-node at air/semiconductor interface as well.

2.3 Thermal Management

2.3.1 Need for Thermal Management in VECSELs

Efficient thermal management is vital for all semiconductor lasers. The challenges for thermal management in VECSEL fall under two headings;

- For VECSELs the power scaling limits are set by absolute temperature not by temperature gradients
- Heat density is much higher in VECSEL when compared to other semiconductor and solid-state lasers

The VECSEL devices are sensitive to the operating temperature due to the following reasons. The gain of the quantum wells falls as temperature rises. Also the sub-cavity resonance and the quantum well gain peak shift spectrally with temperature but typically at different rates. The two can walk out of alignment at certain operating temperature which depends on pump-power level. Thus the fundamental objective of heat management in a VECSEL is make sure the temperature rise per unit pump power is minimized.

2.3.2 Strategies for Thermal Management in VECSELs

The as-grown VECSEL structure can be bonded directly to a heat-sink, however for this configuration (Figure 2.8(a)) the heat is removed from bottom of structure. The thick substrate and DBR offer a high thermal impedance on heat flow path from source to heat-sink. The majority of heat is generated in the active region of the VECSELs as this is where the majority of the pump is absorbed. This configuration

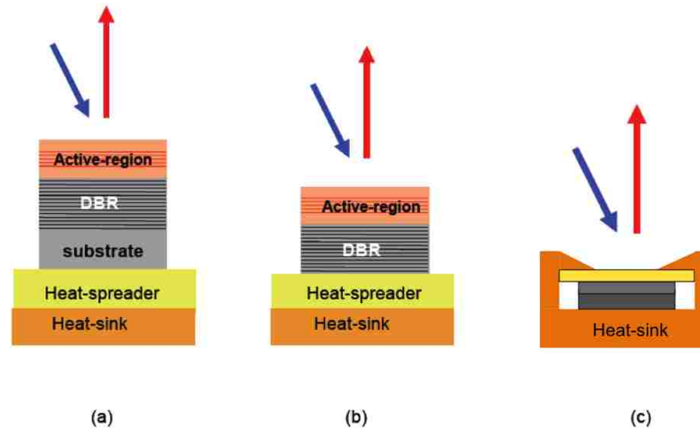

Figure 2.8: Strategies for thermal management for VECSELs.

is good for pulsed-lasing characterization, however CW output power from such a configuration is typically limited to few tens to a few hundreds of milliwatts [19, 20].

The two approaches widely used for heat extraction are;

- Substrate removal to reduce thermal resistance (Figure 2.8(b))
- bonding a transparent heat-spreader to the top surface of the device (Figure 2.8(c))

Each technique has its own pros and cons. Technique (b) depends on availability of good etch stop layers to enable complete substrate removal. III-As VECSELs have high selectivity etch stop layers and etch chemistry which allow complete substrate removal. The III-Sb material system lacks good etch stop layers to allow complete removal of GaSb substrate. Also since the heat is extracted through the DBR layers,

it is desirable that the materials used in DBR fabrication have high thermal conductivity. The DBR effective longitudinal (k_L) and lateral (k_R) thermal conductivities are given by following expressions[21, 22];

$$k_L = \sum_i t_i / \sum_i t_i/k_i \, , \tag{2.22}$$

$$k_R = \sum_i k_i t_i / \sum_i t_i \, , \tag{2.23}$$

where the sums are calculated over all the layers of thickness t_i and thermal conductivity k_i of ith layer. The thermal conductivities of GaAs/AlAs (DBR layers typically grown on GaAs substrates) and GaSb/AlAsSb (DBR layers typically grown on GaSb substrates are listed in Table (2.2).

Table 2.2: Thermal Conductivities at 300K for typically used DBR layers.

Layer	Lattice Match (Substrate)	k (W/mK)
GaAs	GaAs	45
AlAs	GaAs	91
GaSb	GaSb	33
$AlAs_{0.08}Sb_{0.92}$	GaSb	9.8

Technique (c) relies on bonding a high thermal conductivity transparent material to top of the VECSEL for extraction of heat from the active region. The heat spreaders are typically bonded using liquid assisted capillary bonding[23]. The use of a very high thermal conductivity materials such as diamond or SiC, bypasses the thermal resistance of the DBR structure and enables higher power operation for devices grown on substrates with low thermal conductivity. However the ability to efficiently extract heat relies on formation of a good capillary bond between the VECSEL top layer and heat spreader. However intra-cavity heat spreader introduces scattering losses and effects the VECSEL emission spectrum due to etalon effects.

2.4 2 μm VECSEL Devices

2.4.1 Choosing the III-Sb alloys for $\sim$ 2μm operation

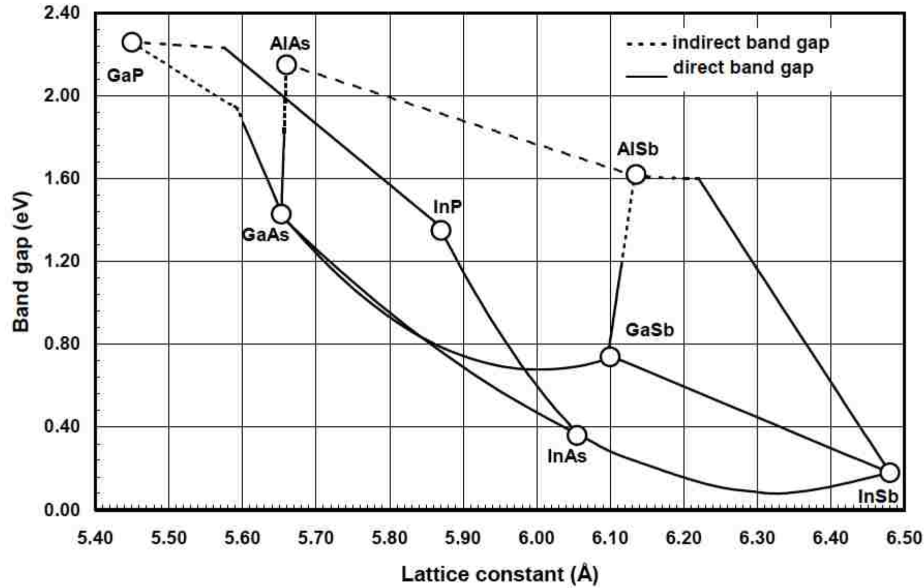

Figure 2.9: Band gaps and lattice constants for III-V semiconductors at room temperature.

In order to choose materials best suited for a 2μm VECSEL structure, important properties such as band gap energies and lattice constants must be considered. The VECSEL emission wavelength and constituent layers influence the choice of substrate on which these materials can be grown epitaxially with low defects. For $\sim$2μm operation GaSb is the substrate of choice. From the III-V band gap vs lattice constant chart (Figure 2.9), the components of VECSEL (DBR layers, barrier, active region, clad region etc.) are chosen so as to minimize lattice mismatch with the GaSb substrate. The lattice constants of the III-V materials used in this study follow Vegards law. For a ternary material like $Al_xGa_{1-x}Sb$ the lattice constant is: $a_{AlGaSb} = x.a_{AlSb} + (1-x).a_{GaSb}$

The ternary alloy $Al_xGa_{1-x}Sb$ is chosen as one of material for barrier layer in III-Sb based VECSELs. The quantum well layers in both VECSELs can either consist of ternary ($In_xGa_{1-x}Sb$) or quaternary alloys ($In_xGa_{1-x}As_ySb_{1-y}$). For emission in the wavelength below 2.1 μm, $Ga_xIn_{1-x}Sb$ QWs are favored. For DBRs GaSb and AlAsSb (lattice-matched to GaSb) are chosen, as they have high index contrast.

2.4.2 2 μm gain region

The VECSEL active region for near 2 μm operation consists of Type-I $Ga_{0.8}In_{0.2}Sb$ QWs embedded in $Al_xGa_{1-x}Sb$ barriers. The semiconductor Bloch equations [24, 25] are used to calculate the absorption, gain and carrier induced refractive index changes in the quantum wells and barrier layers. The modeled and experimental photoluminescence for three different barrier compositions are shown in Figure 2.10, these simulations are done using Simulase software from NLCSTR[26]. The optimum-PL emission is using $Al_{0.25}Ga_{0.75}Sb$ barrier or high-barrier composition. Further growth optimizations and structure optimizations are discussed in detail in Chapter 3.

2.4.3 Fabrication issues with III-Sb mirrors and thermal management.

The DBR for III-Sb VECSELs typically consists of lattice matched AlAsSb/GaSb layers. As discussed in section 2.2.3 the index-contrast (Δn) between lattice matched $AlAs_{0.08}Sb_{0.92}Sb$ and GaSb layers is ~ 0.515 at a design wavelength, $\lambda_{\text{Design}} = 2.0$ μm. For obtaining reflectivity (R_{DBR}) $\geq 99\%$, the minimum number of $\lambda/4$ thick DBR pairs needed is 19 or 20, which correspond to thickness of 5.44 μm and is typically grown using molecular beam epitaxy (MBE). The details about MBE growth of III-

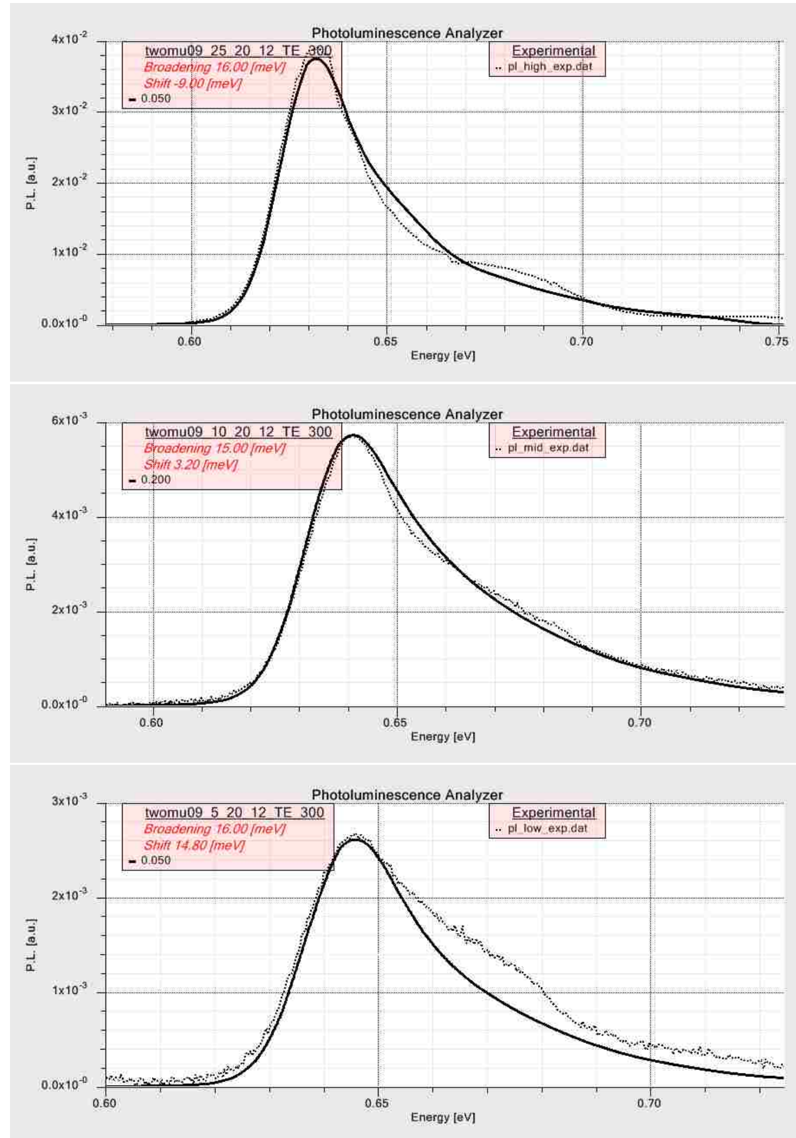

Figure 2.10: Experimental and Theoretical comparison of PL for $Ga_{0.8}In_{0.2}Sb$ QW and three different barrier compositions (top) barrier: $Al_{0.25}Ga_{0.75}Sb$ (middle) barrier: $Al_{0.10}Ga_{0.90}Sb$ (bottom) barrier : $Al_{0.05}Ga_{0.95}Sb$.

Sb DBRs are discussed in section. 3.2.3. The surface quality of such thick epitaxial layers depends on several parameters;

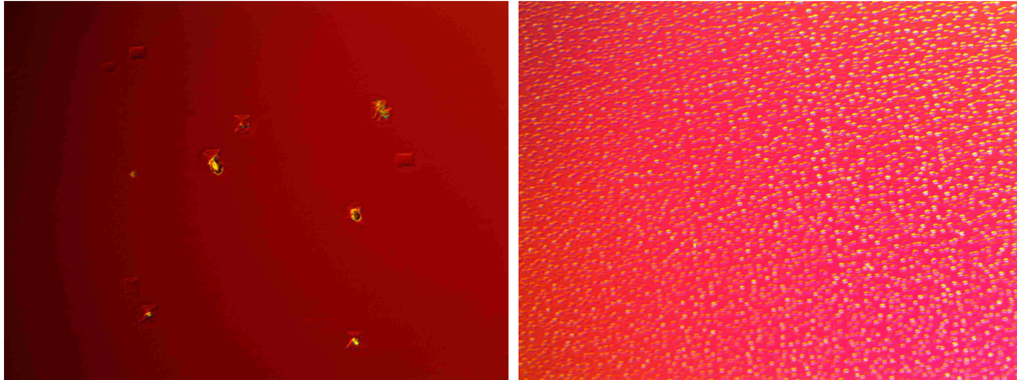

Figure 2.11: Pyramidal defects on surface of GaSb/AlAsSb DBRs grown on different substrates (left) n-doped GaSb substrate (right) Un-doped GaSb substrate.

- Lattice-matching of AlAsSb layer to GaSb substrate
- wafer-surface quality
- III-V flux ratio during MBE growth
- growth temperature of epitaxial layers
- proper removal of oxide from epi-ready wafer surfaces

The GaSb substrates used during MBE growth can vary a lot in their surface quality and controlled oxide thicknesses from batch to batch. Parameters such as lattice-matching, III-V flux ratios, growth temperature and oxide-removal temperatures can be optimized. Figure 2.11 (left) shows presence of widespread pyramidal defects on surface of an epitaxially grown III-Sb DBR grown on a GaSb (n-type) substrate. The density of such pyramidal-defects also depends on the growth temperature of homo-epitaxial GaSb layer grown after oxide-desorption from GaSb wafer surface. The defects are more prominent for un-doped GaSb substrates (Un-GaSb) when compared to similar growth on n-doped GaSb substrates (shown in Figure 2.11

(right)). Thus quality control of surface defects is dependent on the GaSb wafer fabrication steps and it is therefore an uncontrolled parameter during epitaxial growth of III-Sb VECSELs grown on GaSb substrates.

Also as discussed in Section 2.3, efficient thermal management schemes are crucial for high-power operation of VECSEL devices. The thermal conductivities of AlAsSb and GaSb layers are typically much lower when compared to III-As layers, thus only viable option for heat extraction from III-Sb VECSELs is to bond a transparent diamond heat spreader on top-layer of device (Figure 2.8(c)), thus having a good surface-quality is much more crucial in these devices.

2.5 Need for alternate substrate for 2 μm VECSEL growth

The III-Sb VECSELs grown on GaSb substrates suffer from few issues which are a bottleneck towards high-power operation of these devices, some of the important issues are;

- Surface Defects: can depend on wafer quality and type
- low-thermal conductivity of DBR layers (AlAsSb/GaSb) : due to this only option for heat extraction is transparent heat spreader bonded on top of the III-Sb VECSEL surface
- No etch stop layer : GaSb-substrate cannot be removed reliably for III-Sb VECSELs grown on GaSb substrates

The III-As material system has a mature substrate removal technology that permits the complete substrate removal and therefore the diamond heat spreader can

be moved out of the cavity and onto the DBR. III-Sb lack such effective etch stop layers, which along with poor thermal conductivity of III-Sb DBRs have restricted these lasers to thermal management schemes requiring intra-cavity heat spreading. The use of intra-cavity heat spreaders such as transparent diamond invariably leads to stimulated photons in the cavity interacting with defects in the diamond, enough to restrict the performance of the lasers. Thus, the ability to grow an antimonide active region on a III-As DBR on a substrate with an established etch stop recipe such as GaAs or InP could lead to significant improvements in the thermal management of the antimonide lasers and consequently much higher values for the maximum CW output power from the VECSELs.

One such strategy to achieve antimonide VECSELs on GaAs would be develop the growth of antimonide active regions on GaAs substrates which would allow for complete substrate removal without the need for an etch stop layer. A citric acid based etch has a high selectivity between GaSb and GaAs and can thus result in complete removal of the substrate. However the main issue with this approach is the 7.78% mismatch that exists between the GaSb and the GaAs binaries, which could lead to extensive threading dislocations in the GaSb epilayer and hence result in overwhelming non-radiative recombination losses in the antimonide active region. Furthermore, if the growth of the antimonide active region is done on a GaAs substrate, the first quantum well is typically within 500 nm of the mismatched interface. Thus, apart from the issue of excessive threading dislocations the issue of non-reproducible relaxation in the antimonide buffer also needs to be addressed. If the antimonide buffer does not relax reproducibly, then the in-plane lattice constant of the buffer will change from growth to growth, also affecting the quantum well strain between growths. Such issues lead to performance degradation in edge-emitters, however in a vertical cavity laser the position of the gain-peak and the micro-cavity resonance must be precise, and variation in the gain peak is much more catastrophic. Thus any metamorphic buffer based approach has to result in two conditions in the active

region

- the antimonide layer should have the minimum possible threading dislocation density
- the buffer must have a highly reproducible lattice constant with preferably a 100% relaxation

References

[1] Rahsid Safaisini, *Impact of thermal management on VERTICAL-CAVITY SURFACE-EMITTING LASER (VCSEL) power and speed*, Dept. of Electrical and Computer Engineering, Colorado State University, Fort Collins, 2011.

[2] O.G. Okhotnikov, *Semiconductor Disk Lasers:Physics and Technology*, Weinheim, Germany: Wiley-VCH Verlag GmbH & Co. KGaA, Apr. 2010.

[3] Coldren, L.A. and Corzine, S.W., *Diode Lasers and Photonic Integrated Circuits*, John Wiley & Sons, Inc., New York, 1995.

[4] Li, H. and Iga, K. *Vertical- Cavity Surface-Emitting Laser Devices*, Springer, 2002.

[5] Kapon, E. *Semiconductor Lasers I: Fundamentals*, Academic Press, 1999.

[6] Kapon, E. *Semiconductor Lasers II: Materials and Structures*, Academic Press, 1999.

[7] Diehl, R. High Power Diode Lasers, Springer, 2000.

[8] S. W. Corzine, R. S. Geels, J. W. Scott, R-H Yan, and L. A. Coldren, *Design of Fabry-Perot surface-emitting lasers with a periodic gain structure*, IEEE Journal of Quantum Electronics, vol. 25, pp.1513-1524, 1989.

[9] M. Y. A. Raja, S. R. J. Brueck, M. Osinski, C. F. Schaus, J. G. McInnery, T. M. Brennan, and E. M. Hammons, *Resonant periodic gain surface-emitting semiconductor lasers*, IEEE Journal of Quantum Electronics, vol. 25, pp.1500-1512, 1989.

[10] M. Kuznetsov, F. Hakimi, R. Sprague, and A. Mooradian, *High-power (> 0.5-W CW) diode-pumped vertical-external-cavity surface-emitting semiconductor lasers with circular TEM_{00} beams*, Photonics Technology Letters, IEEE, 9(8):10631065, Aug. 1997.

[11] A. R. Zakharian, J. Hader, J. V. Moloney, S. W. Koch, P. Brick, S. Lutgen, *Experimental and theoretical analysis of optically pumped semiconductor disk lasers*, Applied Physics letters, vol. 83, pp 1313-1315, 2003.

[12] B. Rsener ; N. Schulz ; M. Rattunde ; C. Manz ; K. Khler, et al. *GaSb-based VECSEL exhibiting multiple-watt output power and high beam quality at a lasing wavelength of 2.25 μm*, Proc. SPIE 6997, Semiconductor Lasers and Laser Dynamics III, 699702, April, 2008).

[13] Rosener, B.; Schulz, N.; Rattunde, M.; Manz, C.; Kohler, K.; Wagner, J., *High-Power High-Brightness Operation of a 2.25 μm (AlGaIn)(AsSb)-Based Barrier-Pumped Vertical-External-Cavity Surface-Emitting Laser*, Photonics Technology Letters, IEEE, vol.20, no.7, pp.502,504, April, 2008.

[14] Carl Wilmsen, Henryk Temkin, and Larry A. Coldren, *Vertical-Cavity Surface-Emitting Lasers - Design, Fabrication, Characterization, and Applications.* Cambridge Studies in Modern Optics, 1999.

[15] Babic, D.I. and Corzine, S.W., *Analytic expressions for the reflection delay, penetration depth, and absorptance of quarter-wave dielectric mirrors*. IEEE J. Quantum Electron., 28, 514524, 1992.

[16] Zory, P.S. (ed.),*Quantum Well Lasers*, Academic Press, San Diego, 1993.

[17] Frank H. Peters and W.L. Gore and Associates. *Vertical Version 1.1 Beta*, 1996.

[18] A.R. Albrecht, *InAs quantum dot vertical-cavity lasers*, Ph.D. dissertation, Dept. Phy. Astron., Univ. New Mexico, Albuquerque, 2009.

[19] Holm, M.A., Burns, D., Cusumano, P., Ferguson, A.I., and Dawson, M.D., *High-power diode-pumped AlGaAs surface-emitting laser*. Appl. Opt., 38, 57815784,1999.

[20] Ouvrard, A., Garnache, A., Cerutti, L., Genty, F., and Romanini, D., *Single-frequency tunable Sb-based VCSELs emitting at 2.3 μm.* IEEE Photon. Technol. Lett., 17, 20202022, 2005.

[21] Kemp, A.J., Valentine, G.J., Hopkins, J.M., Hastie, J.E., Smith, S.A., Calvez, S., Dawson, M.D., and Burns, D., *Thermal management in verticalexternal- cavity surface-emitting lasers: finite-element analysis of a heatspreader approach.* IEEE J. Quantum Electron., 41, 148155, 2005.

[22] Kemp, A.J., Valentine, G.J., Hopkins, J.- M., Hastie, J.E., Smith, S.A., Calvez, S., Dawson, M.D., and Burns, D., *Corrections to Thermal management in*

vertical-external-cavity surface emitting lasers: finite-element analysis of a heat spreader approach IEEE J. Quantum Electron., 46, 85, 2006.

[23] Liau, Z.L., *Semiconductor wafer bonding via liquid capillarity*, Appl. Phys. Lett., 77, 651653, 2000.

[24] J. Hader, G. Hardesty, T.-L. Wang, M.J. Yarborough, Y. Kaneda, J.V. Moloney, B. Kunert, W. Stolz, and S.W. Koch, *Predictive Microscopic Modeling of VECSELs*, IEEE J. Quantum Electron. vol. 46, pp. 810-817, 2010.

[25] M. Lindberg and S.W. Koch, *Effective Bloch Equations for Semiconductors*, Phys. Rev. B vol. 38, pp. 3342 - 3350, 1988.

[26] *SimuLase software is a product of Nonlinear Control Strategies Inc. See www.nlcstr.com for details.*

Chapter 3

MBE growth and Optimization of VECSEL structures.

Epitaxial growth and wafer characterization are key processes for obtaining high performing VECSEL devices. This chapter introduces the epitaxial growth process, optimization of VECSEL active and DBR regions, and characterization techniques such as Photoluminescence, AFM, X-Rays diffraction analysis and Reflectivity measurements.

3.1 Epitaxial Growth

MBE is used for epitaxial growth of VECSEL structures described in this thesis. Epitaxial growth of III-Sb VECSEL structures is a complicated process and depends on optimization of several parameters simultaneously such as growth rate, flux ratios and growth temperatures. The type and quality of substrates used during MBE growth can also influence VECSEL performance. The epitaxial growth is done in a VG Semicon (V80H) MBE reactor as well as in a Veeco Gen-10 MBE system.

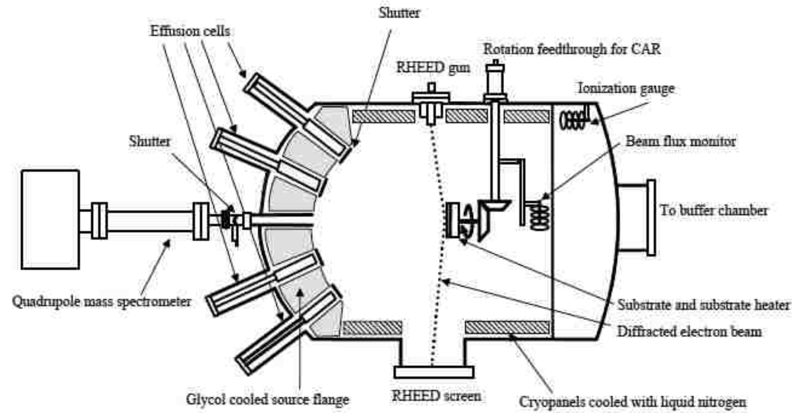

Figure 3.1: Schematic of a MBE growth chamber. (Figure taken from [1])

3.1.1 Molecular Beam Epitaxy

Molecular beam epitaxy (MBE) is a growth technique well suited for growth of complex structures. It can incorporate thin layers of different composition with abrupt interfaces. The structures grown using MBE are typically grown at ~ 1 monolayer/second or at even slower growth rates. Relatively low substrate temperatures are used during growth when compared to other epitaxial growth techniques (MOCVD, LPE). Since MBE is not a thermal equilibrium growth technique it allows the growth of layers with metastable compositions[2]. The MBE growth process is performed in an ultrahigh vacuum chamber (background pressure is in the range $10^{-11} - 10^{-10}$ mbar). Figure 3.1 shows the schematic of a MBE growth chamber. The MBE machines at UNM utilize the following sources, Group III (Aluminum, Indium, Gallium), Group V (Arsenic and Antimony), P-dopant (Beryllium), N-dopants (GaTe and Silicon). These very pure materials (typically $\sim$ 99.99999 % pure) are heated in effusion cells to create a flux of atomic or molecular species. Shutters in front of the sources can be opened to release a flux of atoms or molecules towards a heated substrate. The substrate is loaded in a wafer holder which is in close

proximity to a substrate heater, the entire assembly can be rotated during growth. Rotation is needed to reduce the effects of non-uniform flux profile created at the wafer-surface due to angle of sources. The flux of molecules is a function of the cell temperature and the amount of material in the cell. The number of molecules which incorporate in the epitaxial layer depends on the sticking coefficient of the species, growth rate and substrate temperature. Group V species such as As and Sb do not have unity sticking coefficient (i.e. not all the molecules impinging on the substrate surface incorporate into the epilayer).

MBE growth of VECSEL structures is done on GaSb substrates and GaAs/AlGaAs DBRs pre grown MOCVD. The active regions for wavelength calibration and photoluminescence (PL) optimization are grown on GaAs and GaSb substrates. The substrates used for epitaxial growth are typically epi-ready and there is no need to etch the substrates to remove the surface oxides. The substrates are first loaded in the MBE-load lock (entry/exit chamber). From the load-lock they are transferred to the prep-chamber for outgassing. The substrates are outgassed at $\sim$ 200-400 °C for 0.5-2 hours to remove water vapor and other contaminants from the wafer surface. After the initial outgassing the substrate is then transferred to the growth chamber where oxide desorprtion is done before growing any epitaxial layer on the substrate surface. The substrate temperature is ramped up slowly, 10°C/min from 250°C up to the oxide desorption temperature. The substrate is exposed to group V flux (As_2 for GaAs substrates and Sb_2 for GaSb substrates) above 350°C to prevent desorption of group V species from the wafer surface. The substrate temperature is monitored using pyrometry, an optical pyrometer is mounted on a view-port looking directly at the wafer surface. The pyrometer with a response above the band gap of the substrate is used, as it allows the measurement of radiation from the substrate, not radiation being transmitted through the substrate from the heater assembly behind the substrate. An emissivity value of 0.61 is used for GaSb substrates and a value of 0.687 is used for GaAs substrates. When the substrate temperature is close to the

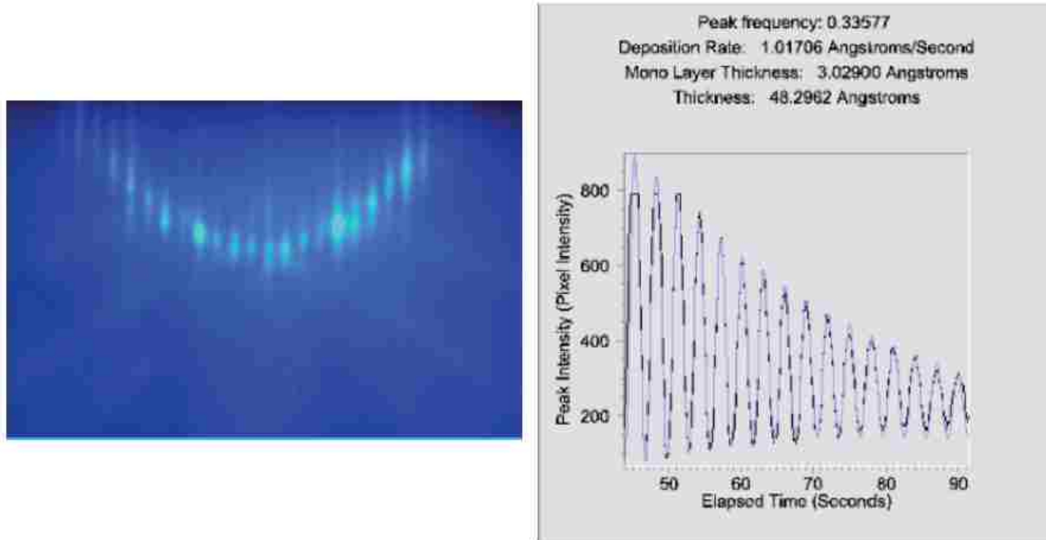

Figure 3.2: (left) 2x4 GaAs RHEED pattern (right) Estimating GaAs growth rate using damped sine fit

oxide desorption temperature, RHEED (Reflection high energy electron diffraction) pattern is used to monitor the surface to see signs of oxide desorption from the wafer surface. The RHEED pattern changes from a diffuse scatter to a clear 3-D RHEED pattern at the oxide desorption temperature. The wafer is then baked at this oxide desorption temperature for $\sim$ 20 minutes and then the substrate temperature is lowered to the growth temperature of the desired epitaxial layer. After growth of less than 100 Å of homo-epitaxial layer the RHEED pattern consists of continuous streaks (Figure 3.2 (left) shows 4x GaAs RHEED pattern).

3.1.2 RHEED calibrations

The GaAs, GaSb and other III-As, III-Sb layers are grown with an overpressure of the respective group V. The growth rate of layers is group-III limited and is

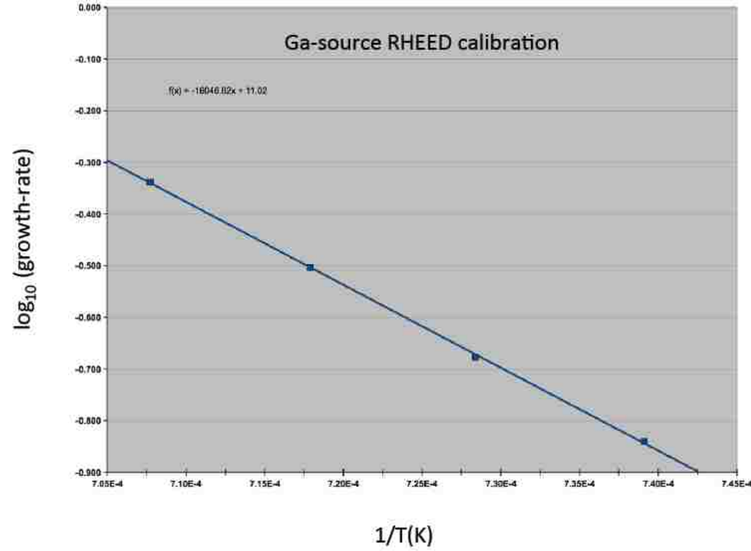

Figure 3.3: Arrhenius plot of GaAs RHEED oscillations.

determined using RHEED intensity oscillations of that particular group-III element species. The intensity variation of the RHEED spot is observed using a camera. For an atomically smooth layer the intensity of the RHEED spot is at its maximum, as the growth commences, islands on the surface of the wafer start to nucleate. Due to nucleation of these islands the wafer surface is now considerably rougher and cannot reflect electron beam very well. After deposition of about half a monolayer, the RHEED intensity is at minimum value. As the growth continues the surface starts to smooth out again, thus the intensity starts to increase again. The RHEED intensity variation for GaAs are shown in Figure 3.2 (right). RHEED calibrations for Ga and Al are done on a GaAs substrate. A small GaAs sample ($\sim$ 5x5 mm) mounted on a Molybdenum plate is typically used as growth-rate calibration sample. One period in RHEED intensity oscillation corresponds to the growth of 1 atomic monolayer. Averaging over a set of 30-40 oscillations, the growth rate at a particular effusion cell temperature can be calculated in monolayers/second. It is advantageous

to use RHEED calibration software which can do Fourier transform or a damped sine-wave fit on oscillation data to obtain accurate growth rates. The log of the measured growth rates are plotted against the inverse of the source temperature (Arrhenius plot). The slope and intercept of a fitting line are used to obtain growth rates at different temperatures and on different substrates. A typical Arrhenius plot of growth rate vs. 1/T(in Kelvin) for Gallium source of the V-80H MBE is shown in Figure 3.3.

3.2 VECSEL growth and Optimization

The VECSEL devices discussed in this dissertation are comprised of an epitaxially grown III-Sb-based active region emitting at or near 2 μm on GaAs/AlGaAs DBRs, which are compared to the same active region grown lattice matched to GaSb/AlAsSb DBRs. Technical challenges related to the MBE growth of VECSEL structures are manifold. First, the IMF based growth of III-Sb on GaAs leads to differences in strain and relaxation of the epilayer when compared to growth on GaSb substrates. This influences the optical emission from the III-Sb active region, since it depends on the compressive strain in the quantum wells. It requires an independent development of the active region, grown on GaAs. Second, the transfer of the IMF growth technology from growth on GaAs substrates to growth on the MOCVD grown AlGaAs/GaAs DBR is nontrivial. The challenges include the IMF formation on the DBR surface, which is slightly rougher than a GaAs substrate surface, and the growth temperature control, since the DBRs heat conductivity differs from that of a GaAs substrate.

3.2.1 Interfacial Misfit Dislocation Array-Based Growth of GaSb on GaAs

The growth of highly mismatched (~ 7.8 %) III-Sb active regions on GaAs/AlGaAs DBRs is based on an interfacial layer of 90° misfit dislocations at the GaSb/GaAs growth interface[3, 4, 5]. The strain mismatch energy between GaSb and GaAs is relieved via formation of misfit dislocations at the interface. A key requirement for the VECSEL structure is that the array of 90° misfit dislocations forms reliably over large areas. The GaSb epi-layer then spontaneously relaxes and its threading dislocation density (TDD) is low. This is important as threading dislocations can introduce a strong non-radiative recombination process [6] in the VECSEL active region and relaxation less than 100% would make the strain in the QWs unpredictable. The low TDD is key to optimized performance from such III-Sb VECSEL active regions grown on GaAs/AlGaAs DBRs.

The MBE growth process of GaSb on GaAs growth is described first for both IMF and non-IMF growth techniques. In IMF based growth of GaSb on GaAs, a GaAs smoothing layer is grown at 580 °C after oxide desorption. After this the substrate temperature is raised to 610 °C and the arsenic-shutter is closed to let As_2 desorb (40 seconds duration) leaving a Ga terminated surface, at this point Sb-flux is impinged on the wafer-surface for a duration of 20 seconds, during this the RHEED pattern changes from 4x2 Ga-stabilized surface to a 2x8 Sb-stabilized surface reconstruction. The substrate temperature is then lowered to the desired growth temperature ($\sim$ 510 °C) under Sb-overpressure and once the substrate temperature stabilizes the Ga-shutter is opened. For the first few monolayers of GaSb growth the RHEED pattern is not well defined and indicates a 3-D growth mode. As growth progresses the GaSb-islands coalesce to form a GaSb layer and a 1x3 RHEED reconstruction pattern is observed after deposition of approximately 30-35 MLs of GaSb. In the case of the non-IMF growth mode, after the oxide desorption and growth of a GaAs smoothing

layer at 580 °C, the temperature is lowered to 510 °C under As-overpressure. Once the growth temperature stabilizes at 510 °C the As-shutter is closed and Ga and Sb shutters are opened simultaneously. For the first few monolayers, GaSb grows in a 3D-growth mode (as observed in RHEED pattern) and as the GaSb growth progresses a well-defined 1x3 RHEED pattern is observed.

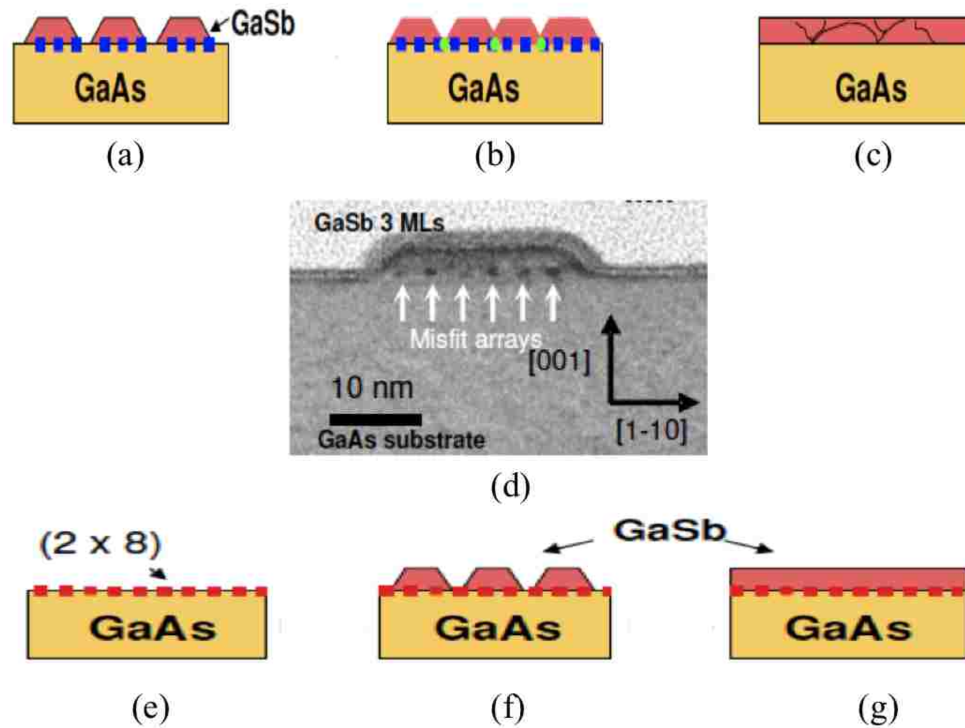

Figure 3.4: (a) Growth of first-few monolayers of GaSb on GaAs (90° misfit dislocations underneath the GaSb islands, (b) Coalescence of islands lead to 60° misfit dislocation which can act as source of threading dislocations, (c) GaSb epi-layer grown with non-coherent coalescence of islands, (d) Cross-sectional TEM image of 100% relaxed GaSb island on GaAs, (e) Sb (2x8) reconstruction on GaAs, (f) Completely relaxed islands of GaSb on GaAs, also shown are coherently linked misfit dislocations underneath these islands, (g) GaSb epi-layer formed as a result of coherently linked misfit dislocations underneath GaSb islands. (Figure taken from [11])

Researchers such as Rocher et. al. [7] have shown that periodic misfit dislocation arrays exist beneath GaSb islands grown on GaAs substrates. The first few

monolayers of GaSb grow on GaAs as 3-dimensional islands, however 90° misfit dislocation arrays exist beneath such islands[3]. These misfit dislocation arrays accommodate the mismatch between GaSb epi-layer and GaAs substrate. These 90° misfit dislocations are spaced uniformly at 56 Å along both [110] and [$1\bar{1}0$] directions. Figure 3.4(a) shows a schematic illustration of epitaxially grown GaSb islands on GaAs substrates, with periodically spaced misfit dislocation arrays underneath such islands. A high resolution cross-section TEM (XTEM) image of a GaSb island is shown in Figure 3.4(d). A periodically spaced misfit dislocation array can be seen along the [$1\bar{1}0$] direction. Such 100% relaxed islands of GaSb typically exist for the first few monolayers of growth. As the epitaxial growth progresses, the islands coalesce to form a bulk GaSb epi-layer. As can be seen in Figure 3.4(b), when two 90° misfit dislocations merge, the periodicity at the point of coalescence is lost. This leads to formation of a 60° misfit dislocation, which have a high probability of threading into the epi-layers grown above such an interface (a schematic illustration can be seen in Figure 3.4(c)). Figure 3.5 is a XTEM image showing failure of the interface and 60° threading dislocations in GaSb epi-layer can also be seen. The density of such threading dislocations is strongly correlated to the island density and more specifically to number of such coalescence sites[8].

Thus to achieve a low threading dislocation density of GaSb on GaAs either the number of coalescence sites have to be significantly reduced or the arrays of 90° misfit dislocations under all islands have to be linked to form a coherent series. One method to form such a coherent series is to use an Sb (2 x 8) reconstruction on the GaAs surface prior to the growth of the GaSb epilayer (Figure 3.4(e)). This is called reconstruction assisted interfacial misfit dislocation arrays. The reconstruction assisted interfacial misfit-dislocation array is a fundamentally unique epitaxial growth mode based on atomic self-assembly of group V ad-atoms on a lattice-mismatched interface. The basic mechanism for the formation of such an interface is the realization of specific antimony surface reconstructions on the GaAs substrate. These

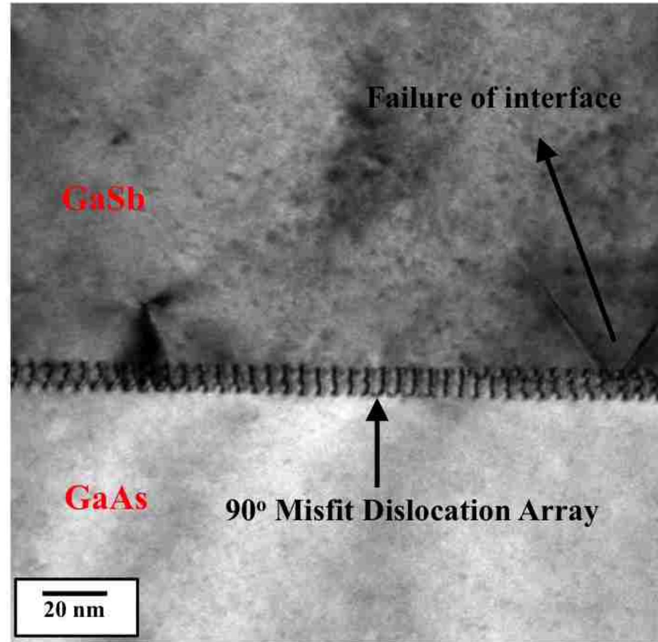

Figure 3.5: HR-TEM Image of GaSb epi-layer on GaAs. Also shown is failure point of the interface and 60° threading dislocations originating from failure point. (Figure taken from [11])

are usually multi-layer reconstructions such as the (2 x 8) Sb reconstruction that surpasses the critical-thickness for the GaSb/GaAs material system without the actual growth of any GaSb. These multi-layer antimony reconstructions are completely strain-relieved and achieve this by forming the 90° misfit-dislocations at the Sb/GaAs interface. The misfit dislocations are spaced uniformly 56Å apart.

This 56 Å periodicity also corresponds to completely relaxed GaSb on GaAs since the spacing is equivalent to 13 lattice sites of GaSb or 14 of GaAs along the [110] and [$1\bar{1}0$] directions and this can be shown to be the best possible ratio for relaxed GaSb on GaAs[4]. The AFM and cross-section TEM image of the IMF based growth of

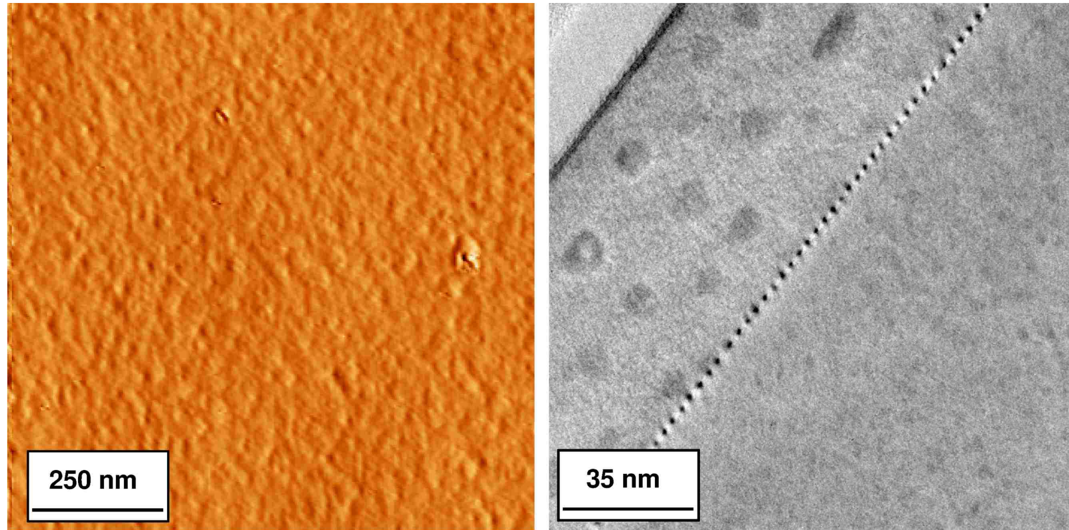

Figure 3.6: (a) Atomic force micrograph of GaSb on GaAs with an optimized IMF array at the GaSb/GaAs interface. (b) cross-section TEM image of GaSb grown on GaAs with a periodic IMF array at the interface. (Figure taken from [12])

GaSb on GaAs is shown in Figure 3.6 (a) and (b) respectively. The AFM shows the complete elimination of screw dislocations while the TEM shows the IMF array and a low threading dislocation density GaSb layer on GaAs. The reconstructions ability to self-assemble and dynamically change its coverage on the substrate allows for a monolayer of completely relaxed GaSb to be realized across the GaAs substrate. At present, a network of such intact misfit dislocations across several square microns in area can be achieved[3]. In theory such a periodic array can exist across the entire GaAs substrate regardless of its diameter. However, steps in the wafer and arsenic intermixing in the Sb reconstruction have restricted these dislocation arrays to a few square microns in area, and threading dislocation densities of 5 x $10^6/\text{cm}^2$ has been observed[9].

Another key requirement for achieving good emission properties from III-Sb active regions grown on GaAs substrates is that the GaSb epitaxial layers grown on GaAs should be $\sim$ 100% relaxed. X-rays diffraction (XRD) is one of the techniques

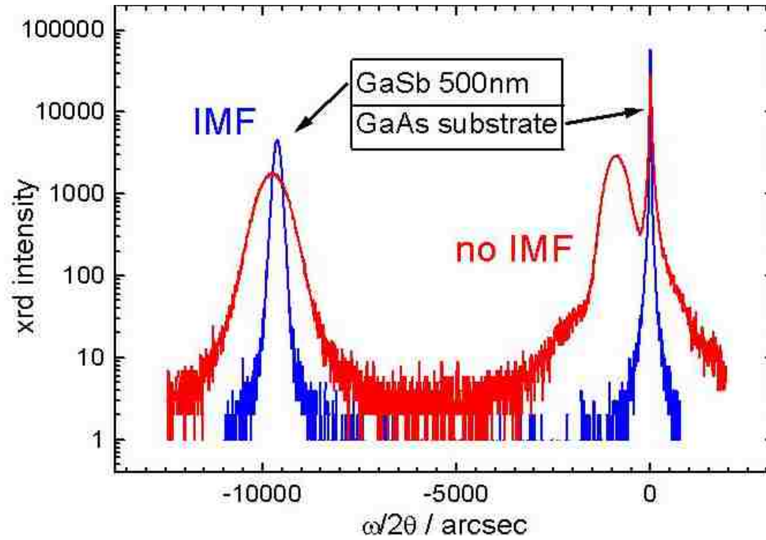

Figure 3.7: XRD (004) scan of a 0.5 μm GaSb on GaAs substrate grown using IMF and non-IMF growth mode. (Figure taken from [5])

to measure the relaxation of epitaxial layers. The $\omega - 2\theta$ symmetric (004) XRD spectra for a 500nm thick GaSb epitaxial layers and deposited using IMF and non-IMF growth mode are shown in Figure 3.7 (a) (b), respectively. The full width at half maximum (FWHM) of the non-IMF grown GaSb is significantly broader when compared to the FWHM of the IMF grown GaSb. The non-IMF scan also shows the presence of an additional peak near the GaAs substrate peak. This additional peak is attributed to tetragonally distorted GaSb. During non-IMF growth, initially the in-plane lattice constant of the epitaxial layer and of the substrate are equal up to critical thickness. Afterwards the epitaxial layer slowly relaxes to the GaSb lattice constant via formation of misfit and other threading dislocations (60° or mixed dislocations). Such tetragonal distortion is absent in IMF-grown GaSb epitaxial layers. The calculations based on the symmetric (004) and asymmetric (115) XRD measurements show approximately 98.5% relaxation of the GaSb epitaxial layer. The broad FWHM (194 arcsecs) of GaSb layers, thinner than 1 μm, as shown in Figure 3.7 is due to the small amount of residual strain (less the 2%) in the epitaxial layers after

the creation of the IMF array[4].

3.2.2 Optimization of IMF based Quantum Wells

The quantum well emission wavelength depends on the In content and the thickness of the $Ga_{1-x}In_xSb$ quantum wells. At typical growth temperatures (460-500°C), the reevaporation of indium from the substrate is not negligible, thus the actual In content of the quantum well material depends not only on the nominal In flux but also on the growth temperature. Furthermore, the quantum well emission wavelength and strength depends on its strain. The optical quality of the quantum wells depends on their growth temperature. Finally the Sb flux supplied during growth of the active region becomes important with increasing III-Sb layer thickness, which is also growth temperature dependent. Thus the quantum wells have to be optimized with respect to nominal In content, thickness, as well as growth temperature and Sb flux. The photoluminescence (PL) intensity is used as an optimization parameter, as it is a good measure for the material's optical quality.

Table 3.1: Basic structure of III-Sb based quantum well active regions for PL studies, grown on a GaAs substrate using the IMF.

Layer no.	Composition	Description	thickness	repeats
16	GaSb	cap	10 nm	1X
15	AlSb	barrier	50nm	
14	$Al_{0.3}Ga_{0.7}Sb$	absorber/spacer	80nm	
7	$Al_{0.3}Ga_{0.7}Sb$	absorber/spacer	20 nm	4X
6	$Ga_{1-x}In_xSb$	quantum well	t	
5	$Al_{0.3}Ga_{0.7}Sb$	absorber/spacer	100 nm	1X
4	AlSb	barrier	50 nm	
3	GaSb	buffer	500 nm	
2	IMF			
1	GaAs	smoothing layer		
0	GaAs substrate		$\sim 350\mu m$	

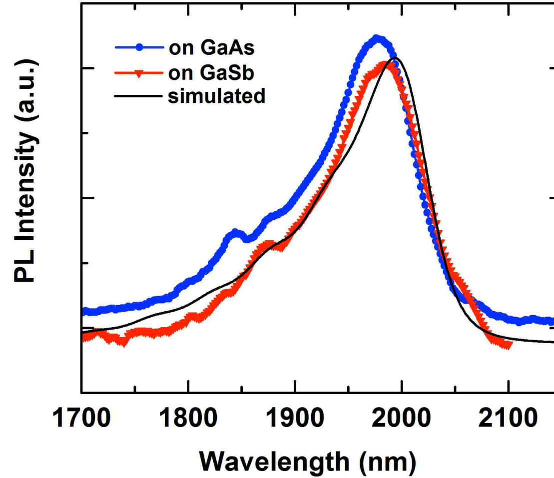

Figure 3.8: PL of a structure with 11 nm thick $Ga_{0.75}In_{0.25}Sb$ quantum wells, grown on a GaAs substrate (blue), and grown on a GaSb (red). For comparison a simulated PL spectrum for $Ga_{0.75}In_{0.25}Sb$ quantum wells is included (black). (Figure taken from [12])

The active region is shown schematically in Table 3.1. It consists of $Ga_{1-x}In_xSb$ quantum wells, separated by 20 nm thick $Al_{0.3}Ga_{0.7}Sb$ spacers, that absorb the pump light. The carriers in the active region are confined by an AlSb barrier. Test samples with four quantum wells are grown for photoluminescence (PL) studies. The test structures have been grown on GaAs, using the interfacial misfit (IMF) array. For comparison test structures are grown directly on GaSb also (starting with layer 3 in Table 3.1). Figure 3.8 shows the PL of test structures with an 11nm thick $Ga_{0.75}In_{0.25}Sb$ well, grown on GaAs and on GaSb. The PL intensity from the sample grown on GaAs exceeds the one from the sample grown directly on GaSb by 20%, indicating that the material grown on GaAs is not significantly inferior to the material grown directly on GaSb. A simulated PL spectrum (using Simulase software) shows good agreement with experimental data at T=290K and a carrier density, N=2.5 x 10^{11} /cm^2. Small differences in strain between antimonide layers grown on GaAs with the interfacial layer of 90° misfit dislocations as compared to those grown on

GaSb can influence the strain in the quantum wells. This influences the optical emission from the III-Sb active region (PL peak wavelength and intensity), since it depends on the compressive strain in the quantum wells. Therefore the active region for growth on GaAs has to be developed independently from that for GaSb.

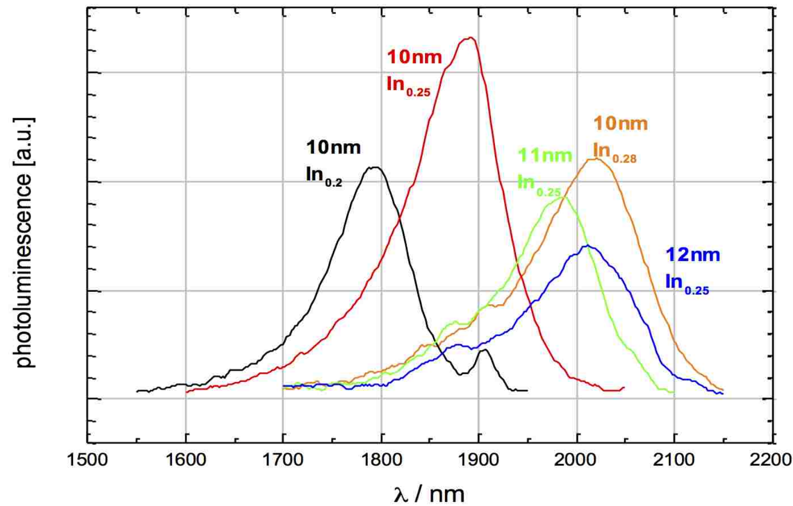

Figure 3.9: PL of several structures as in Table 3.1 with quantum wells of varying thickness and In content. For a $Ga_{0.75}In_{0.25}Sb$ well the emission wavelength can be tuned to 2 μm by increasing the well thickness to 12 nm, but the intensity drops significantly compared to a 10 nm thick well. Higher PL intensity near 2 μm wavelength can be achieved with a 10nm thick quantum well with 28% In content.

Experimental results, in agreement with theoretical modeling, show that the PL peak intensity of $Ga_{0.75}In_{0.25}Sb$ quantum wells of different thicknesses reaches a maximum near 1.9 μm (for 10 nm wide well) and decreases toward longer wavelengths (2 μm for 12 nm wide wells). Higher PL intensities at 2 μm wavelength can be reached with increased In content in the quantum wells (Figure 3.9).

Figure 3.10 shows the influence of the growth temperature. Samples a and b have nominally the same quantum wells (10 nm wide $Ga_{0.72}In_{0.28}Sb$), but are grown at different temperatures, 475 °C and 490 °C, respectively. The emission wavelength of b,

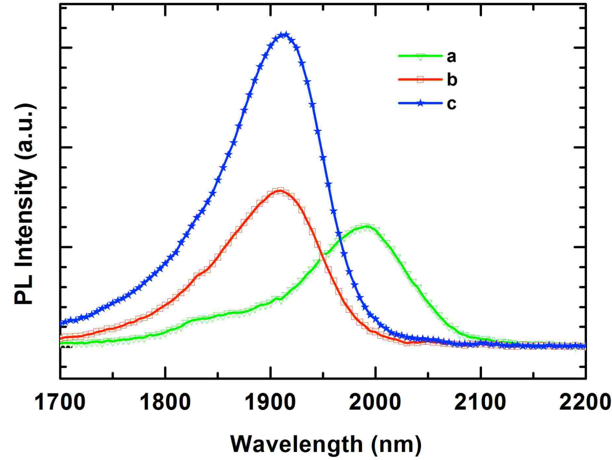

Figure 3.10: PL of a structure with 10 nm thick $Ga_{0.72}In_{0.28}Sb$ quantum wells, grown at 475 °C (a), and at near 490 °C (b). For comparison the emission wavelength of b can also be achieved by a structure with 12 nm thick $Ga_{0.72}In_{0.28}Sb$, grown at 475°C (c). (Figure taken from [12])

grown at a higher temperature, is blue shifted by about 85 nm, and is approximately 30% stronger than a. The blue shift can be attributed to In re-evaporation, which increases at higher growth temperature. On the other hand, the shorter emission wavelength of b can also be achieved by growing a 12 nm thick $Ga_{0.8}In_{0.2}Sb$ well at 475 °C(sample c), yielding more than twice the peak PL intensity. The 12nm thick $Ga_{0.8}In_{0.2}Sb$ quantum well (sample c) contains less In, than the 10 nm wide $Ga_{0.72}In_{0.28}Sb$ well (sample a), which explains the wavelength shift between a and c. The change in intensity between samples b and c is due to differences in material quality, which depend on the growth temperature.

The optimal growth temperature of the quantum wells for an emission wavelength near 2 μm was determined to be 470°C. The layers prior to the first quantum well can be grown at higher temperature, e.g. 510°C for III-Sb, and 580°C for the III-As. Beginning with the first quantum well and all following layers must be grown at

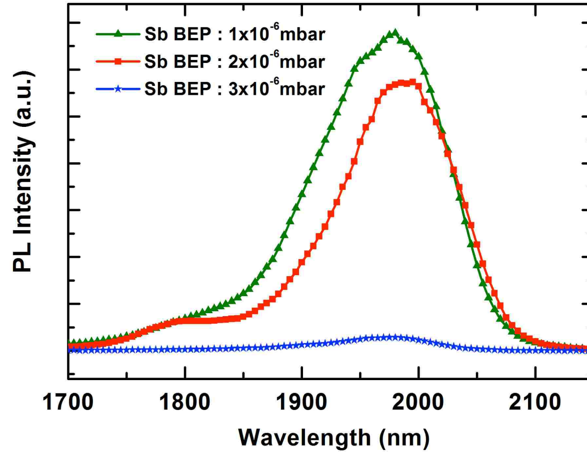

Figure 3.11: Influence of the Sb flux, measured as beam equivalent pressure (BEP) on the PL of a VECSEL active region with 9 quantum wells (grown on GaAs). (Figure taken from [12])

low temperature to avoid deterioration of the GaInSb quantum well; an effect which unlike GaInAs QWs in III-As, will occur even if the temperature is increased after they are already buried in AlGaSb.

For the growth of the entire active region, with 9 quantum wells, the optimization of the Sb flux during growth becomes important. The PL intensity increases by 17x when the Sb flux was reduced from 3 x 10^{-6} mbar to 1 x 10^{-6} mbar (see Figure 3.11). Generally, the PL intensity rises with lower Sb flux, until a minimum Sb flux, below which the substrate surface becomes group III rich and turns hazy. This minimum Sb flux depends on the growth temperature. The minimum Sb:Ga flux ratio is about 2.5 for growth temperatures near 470 °C. The PL optimization resulted in two quantum well designs, 10nm $Ga_{0.72}In_{0.26}Sb$ quantum wells in $Al_{0.3}Ga_{0.7}Sb$ barriers and 13 nm $Ga_{0.8}In_{0.2}Sb$ quantum wells in $Al_{0.25}Ga_{0.75}Sb$ barriers.

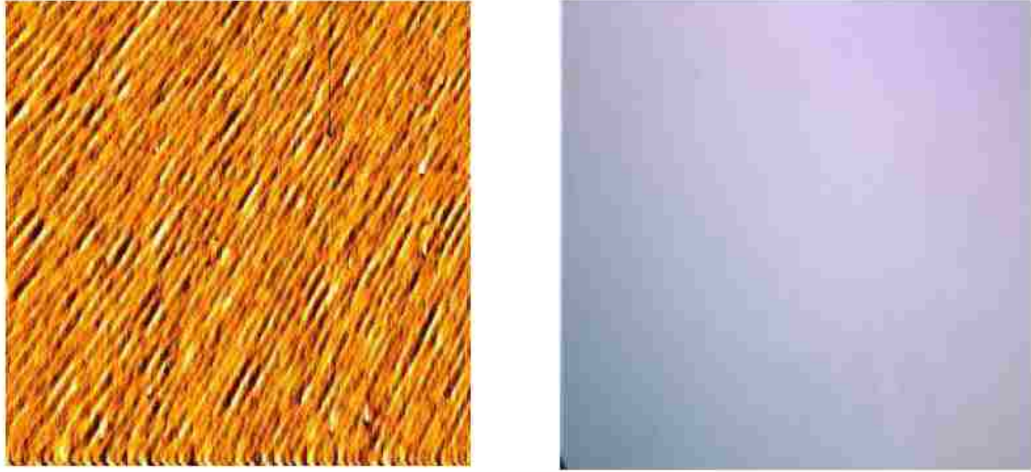

Figure 3.12: left: AFM (5 μm x 5 μm) of GaAs/AlGaAs DBRs with surface roughness $\sim$ 0.3 nm (r.m.s.), right: Nomarski image showing extremely low surface defect density for optimal optical pumping.

3.2.3 Distributed Bragg Reflector: Growth and Characterization

For the LMM-VECSEL (III-Sb VECSELs grown on GaAs/AlGaAs DBRs) the active region is to be grown on a GaAs based DBR. The III-As DBR is grown by MOCVD on a GaAs wafer. For optimum growth conditions in MOCVD a 2° miscut GaAs substrate is used. The III-As DBR design parameters and constituent layers have been discussed in section 2.2.3. Figure 3.12 shows an AFM surface scan and a Nomarski micrograph of the III-As DBR surface. The surface roughness is 0.3 nm (r.m.s.), determined using an AFM scan of the DBR surface. This is slightly higher than 0.18 nm of a typical GaAs wafer surface. The primary issue will be to establish conditions for a good IMF formation on the III-As DBR surface.

The DBR for the LM-VECSEL (III-Sb VECSELs grown on GaSb/AlAsSb DBRs) is grown on a GaSb substrate. The III-Sb DBR consists of 19 pairs of AlAsSb/GaSb

Figure 3.13: Nomarsky image showing crosshatching of surface when AlAsSb epi-layer is not lattice matched to GaSb substrate.

layers. The thickness of epitaxially grown III-Sb DBR is 5.441 μm. A slight lattice mismatch (epi-layer position w.r.t GaSb substrate peak more than $\pm$ 300 arcsecs) can cause crosshatching of the DBR surface. Figure 3.13 shows a nomarski image of a crosshatched DBR surface. The AlAsSb layer in this DBR is $\sim$ 500 arcseconds compressively strained w.r.t GaSb substrate. The active region grown on such a crosshatched surface will also be significantly crosshatched. The crosshatching of the surface prevents the capillary bonding of diamond with VECSEL surface. The lattice matching of AlAsSb layer to GaSb substrate is a sensitive process and depends on parameters such as growth temperature, As:Sb overpressure and group III growth rate. The AlAsSb layer in this example is grown at a temperature of 510 °C at a growth rate $\sim$ 0.5 monolayers/sec.

The As:Sb overpressure is adjusted by controlling the As valve-openings (Sb-flux is kept constant at value reasonable for growth of GaSb layer). The lattice matching and layer composition is verified using X-ray diffraction comparing symmetric (004)

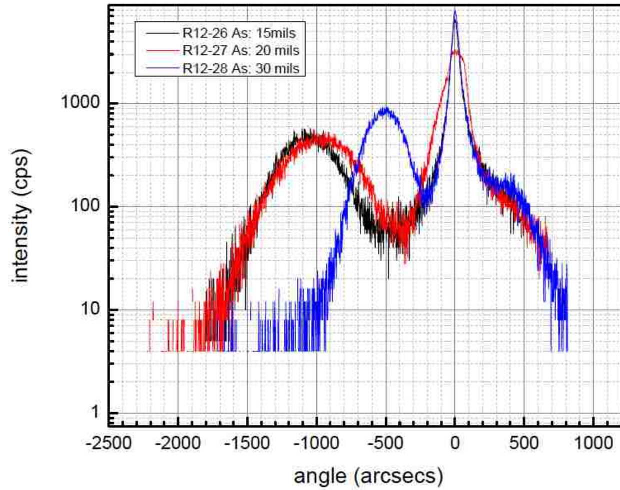

Figure 3.14: (004) X-rays diffraction scan for AlAsSb layers for various As-valve openings. While keeping Sb-flux constant As-flux is increased for each growth to achieve lattice-matching with GaSb substrate.

and asymmetric (115) scans. Figure 3.14 shows (004) X-rays diffraction scan for AlAsSb layers for various As-valve openings. As can be seen in Figure 3.14, increasing the As-flux while keeping Sb flux constant during growth, results in the AlAsSb epi-peak moving closer to GaSb peak. The AlAsSb layer is said to be lattice matched when AlAsSb epi-peak is within ± 100 arcseconds of GaSb substrate peak. Figure 3.15 shows good surface quality without any visible crosshatching (left) and lattice-matching within ± 50 arcsecs (right). The III-Sb DBR (consisting of AlAsSb/GaSb layers) grown on GaSb substrate is analyzed for layer thickness estimation using Peaksplit.

3.2.4 VECSEL subcavity design and growth

The VECSEL sub cavity consists of an on-chip DBR mirror and active region grown epitaxially on top of the DBR. Several VECSEL structures based on the results of the

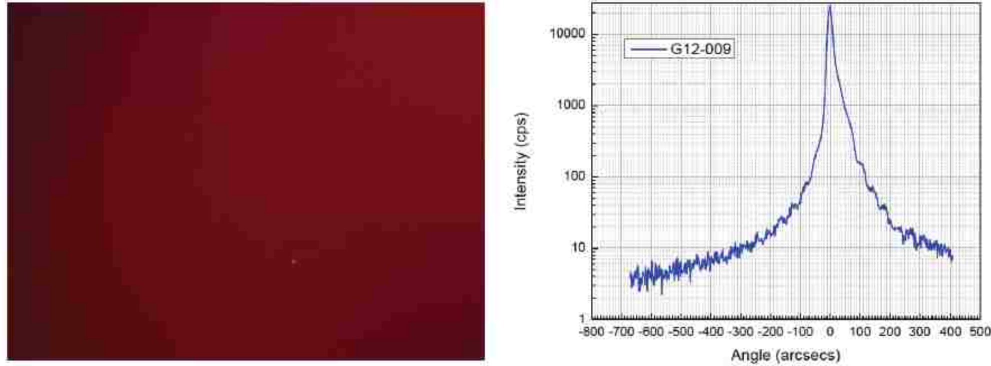

Figure 3.15: (left) Surface nomarsky image of a lattice-matched AlAsSb epilayer (004) X-rays diffraction scan for LM-AlAsSb layer, AlAsSb epi-peak is within $\sim$ 50 arcseconds of the GaSb substrate peak.

active region development and on the DBR development were designed. VECSEL designs were developed that include active regions with 9 QWs and 10 QWs in a RPG type VECSEL subcavity (QWs located at E-field antinodes). These VECSEL active regions were optimized on GaAs substrates for PL characterization. Sample (L8-46) is a LMM-VECSEL active region. It consists of 9 $Ga_{0.8}In_{0.2}Sb$ QW's separated by 266.7 nm thick $Al_{0.3}Ga_{0.7}Sb$ barriers. This separation is designed such that the quantum wells are located at field antinodes of the optical mode associated with the subcavity. The growth conditions were optimized for this structure similar to the 4 QW active region structure discussed in section 3.2.2.

Figure 3.16 shows the photoluminescence of samples with an active region containing 9 QWs grown on a GaAs wafer (L8-46). In comparison to one of the test structures discussed in section 3.2.2 (L7-365), which contained only 4 $Ga_{0.8}In_{0.2}Sb$ QWs, the PL signal has dropped significantly instead of increasing. To understand the reason for this, samples with 4 QWs and wide spacing between the QWs were grown (L8-23 and L8-45 with $Ga_{0.8}In_{0.2}Sb$ QW and separated by 266.7 nm thick $Al_{0.3}Ga_{0.7}Sb$ barriers). The increased PL intensity of these samples (L8-23 and L8-

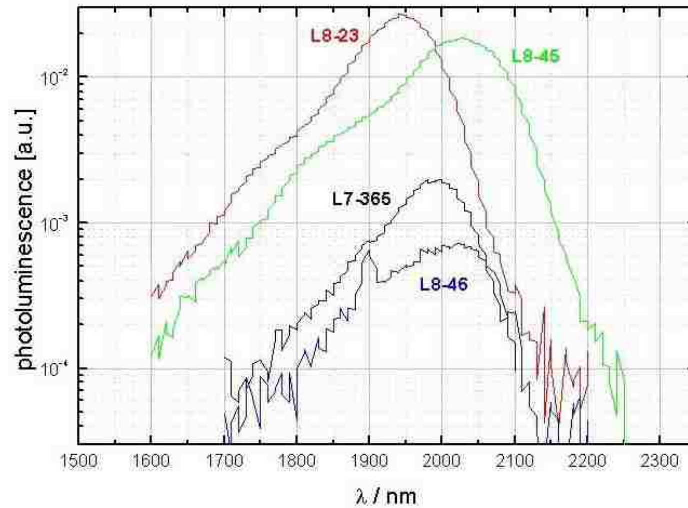

Figure 3.16: L8-23 and L8-45 are active regions with 4 QWs, grown with different growth temperature management which accounts for the wavelength shift. For comparison L7-365 is a similar test structure where the 4 QWs are separated by only 20 nm of $Al_{0.3}Ga_{0.7}Sb$ as in Table 3.1. L8-46 is similar to L8-45, but has 9 QWs.

45) indicates that the accumulated strain of the thick active region degrades the material quality significantly.

Active region structures with 2 and 3 QWs per field antinode were also designed and grown. The PL of these samples indicates that the accumulated strain from the closely spaced QWs degrades the material quality even more than in the structures with 1 QW per field antinode. For this reason active region designs with 1 QW per field antinode is chosen as a basis for VECSEL structure. The growth conditions were then optimized to allow the growth of the IMF and the Sb-based active region on the DBR with comparable material quality to the growth on GaAs substrates.

Based on above optimizations of LMM-VECSEL active regions, a set of VECSEL structures was grown, which includes two quantum well - barrier designs and two different VECSEL subcavity designs. The two quantum well barrier designs are;

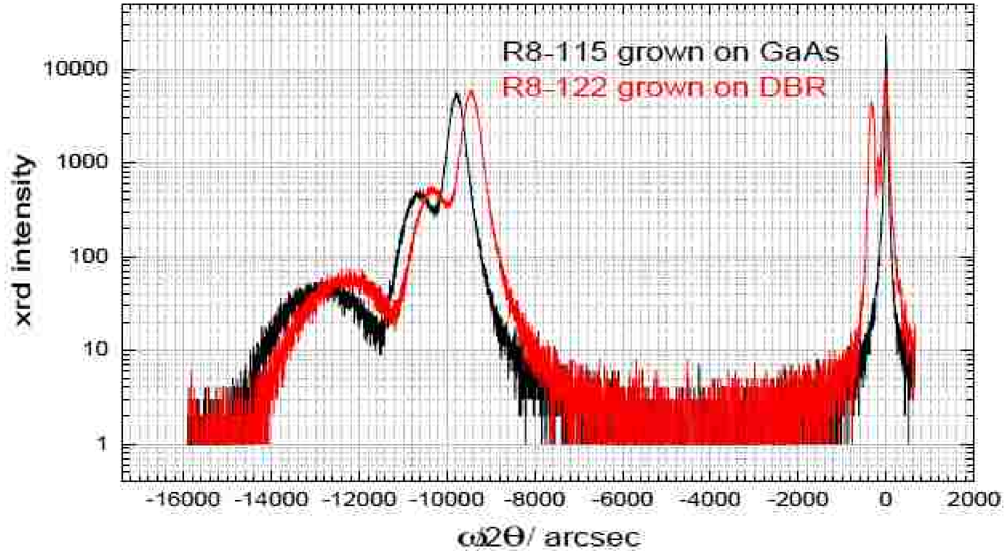

Figure 3.17: X-rays diffraction (XRD) spectra of VECSEL active regions grown on GaAs and grown on the AlGaAs/GaAs DBR. The right most sharp peaks (at 0 arcsec) are the GaAs substrate peaks of both structures. R8-122 (red) shows next to it (at about -400 arcsec) the peak originating from the $Al_{0.95}Ga_{0.05}As$ layers of the DBR. The peaks between -900 and -1100 arcsec indicate the active region's GaSb, AlSb and AlGaSb layers, whereas the wide peaks between -1200 and -1400 arcsec indicate the quantum wells. The angular shift of the III-Sb-peaks between the black and the red curve (active region grown on GaAs and grown on the DBR, respectively) is due to the different surface orientation of the DBR (2° off from (001) toward (011)) compared to the GaAs wafer (001) on which R8-115 was grown.

(a) 10nm $Ga_{0.72}In_{0.28}Sb$ or 10nm $Ga_{0.74}In_{0.26}Sb$ quantum wells in $Al_{0.3}Ga_{0.7}Sb$ barriers

(b) 12nm or 13nm thick $Ga_{0.8}In_{0.2}Sb$ quantum wells in $Al_{0.25}Ga_{0.75}Sb$ barriers

For a growth quality check XRD scans were measured for the VECSEL active regions grown on GaAs as well grown on the AlGaAs/GaAs DBR. Typical 004 scans are shown in Figure 3.17. Good IMF formation is indicated by the absence of any peaks in between the III-As and the III-Sb peaks.

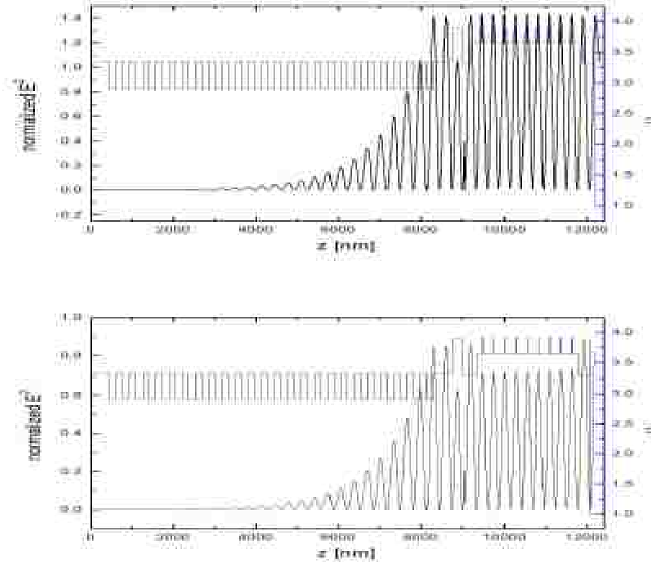

Figure 3.18: Optical field (normalized E^2) and refractive index n inside the VECSEL subcavity. This outlines the difference of the subcavity designs (1) above and (2) below.

The two VECSEL subcavity designs included the above mentioned design, where the quantum wells as well as all refractive index steps (except for the IMF) are located at field antinodes (1) and another design, where only the quantum wells are located at field antinodes and all other refractive index steps are located at field nodes (2). The difference is outlined in Figure 3.18. The first design results in a VECSEL subcavity with higher finesse, the second design with lower finesse. Both the laser structures shown in Figure 3.18 are grown and tested for lasing performance, though the design with 13nm $Ga_{0.8}In_{0.2}Sb$ quantum wells in $Al_{0.25}Ga_{0.75}Sb$ barriers, and the first of the above mentioned subcavity designs, i.e. the quantum wells as well as all refractive index steps (except for the IMF) are located at field antinodes performs better.

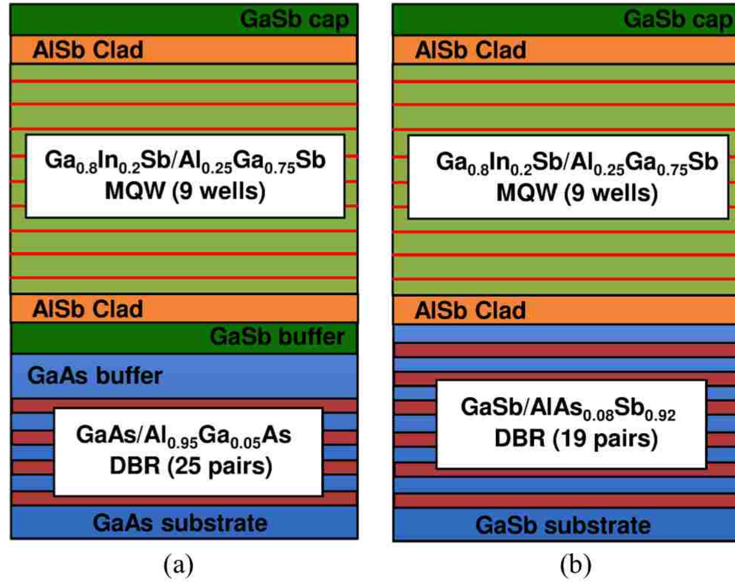

Figure 3.19: (a) Schematic of LMM-VECSEL (b) Schematic of LM-VECSEL (Figure taken from [11])

3.2.5 VECSEL structure growth optimization

As discussed in section 3.2.4 the sub cavity design with 13 nm InGaSb QW and AlGaSb barriers is chosen for the final VECSEL designs. Figure 3.19 shows the schematic of a LM-VECSEL on a GaSb substrate and a LMM-VECSEL grown on a GaAs substrate. These VECSEL structures are grown and optimized before lasing characterization. For optimized device performance it is essential to precisely place the QWs at E-field antinodes within the sub-cavity. This requires precise control of the growth rates of the group-III sources of MBE, as growth rate variation can affect both composition and thickness of the constituent layers.

The quantum well gain region is characterized by its photoluminescence spectrum. The PL spectrum measured normal to the wafer surface is strongly modulated due to the sub cavity etalon and the DBR. The edge-PL spectrum shows significantly

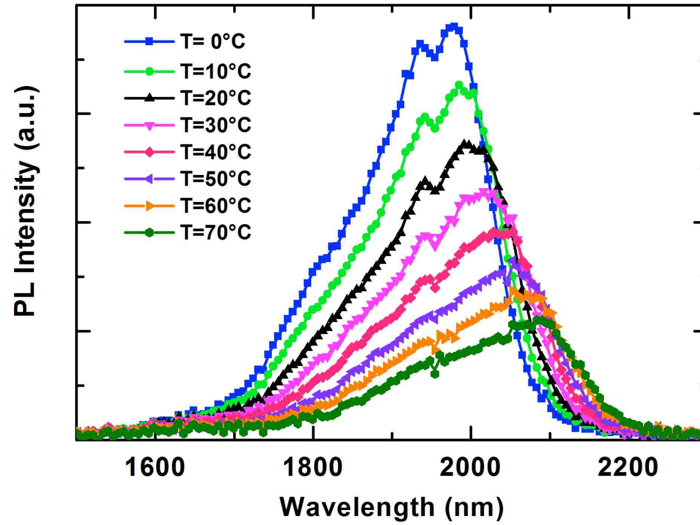

Figure 3.20: Edge PL spectra from a VECSEL sample. (Figure taken from [12])

weaker modulation and is therefore used to determine the QW emissions spectral peak position[6, 10]. The VECSEL sample is mounted on a heat sink to measure the edge/surface PL spectrum at different heat-sink temperatures. Figure 3.20 and 3.21 shows edge and surface PL spectra from a VECSEL sample, respectively. The edge-PL shifts to longer wavelength at about 1.6nm/K [6], primarily due to the bandgap energy dependence on temperature. The sub cavity resonance also shifts to longer wavelength with increasing temperature, but more slowly when compared to the intrinsic gain-peak shift; at about 0.26nm/K. The sub cavity resonance peak shift is due to temperature dependence of refractive indices. The determination of gain-peak and sub cavity resonance shift with respect to temperature is useful in the design of the VECSEL. To achieve high CW output power the gain-peak emission is typically designed to be 30-50 nm shorter than the actual desired wavelength of device operation, such that the gain-peak and sub cavity resonance coincide at the desired operating temperature. The operating temperature depends on pump

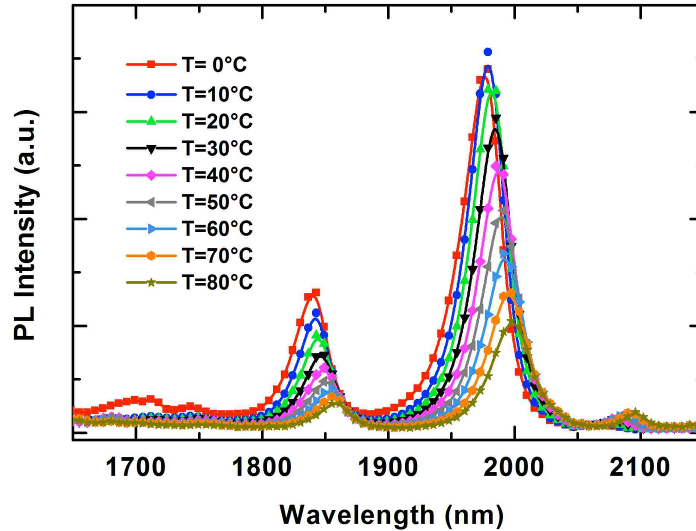

Figure 3.21: Surface PL spectra from a VECSEL sample. (Figure taken from [12])

power, heat-sink temperature and power dissipated in the active region. The target operating temperature for the designed VECSELs is chosen to be ∼ 353K or 80°. The PL emission from InGaSb QWs is optimized for an emission wavelength of ∼ 1950 nm and the subcavity resonance is designed to be ∼ 1990 nm at room temperature.

The reflectivity spectrum is measured using a Fourier transform infrared spectrometer (FTIR) with the VECSEL chip mounted on a heat sink. Figure 3.22 shows the reflectivity spectrum at different heat-sink temperatures. The reflectivity spectrum shows the effect of the sub cavity etalon formed between DBR and air-semiconductor interface. The reflectivity spectrum is used to diagnose the deviation in thickness of layers and composition of both DBR and sub cavity. For the reflectivity spectrum in Figure 3.22 it can be seen that the most optimized overlap between intrinsic QW gain-peak and sub cavity resonance is at a heat sink temperature of 70 °C. This indicates a good agreement between the design and the epitaxially grown

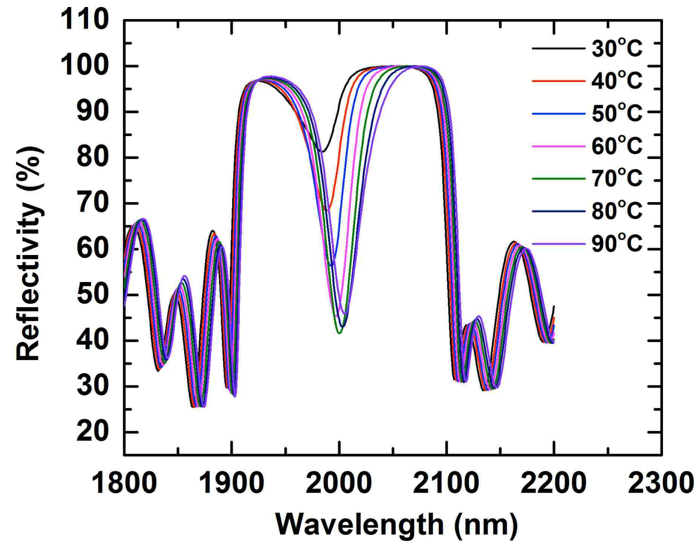

Figure 3.22: Temperature dependent reflectivity (TDR) spectra from a III-Sb VECSEL grown on GaAs/AlGaAs DBR. (Figure taken from [12])

VECSEL sample. However due to growth variations the subcavity-PL alignment can be off as shown in Figure 3.23.

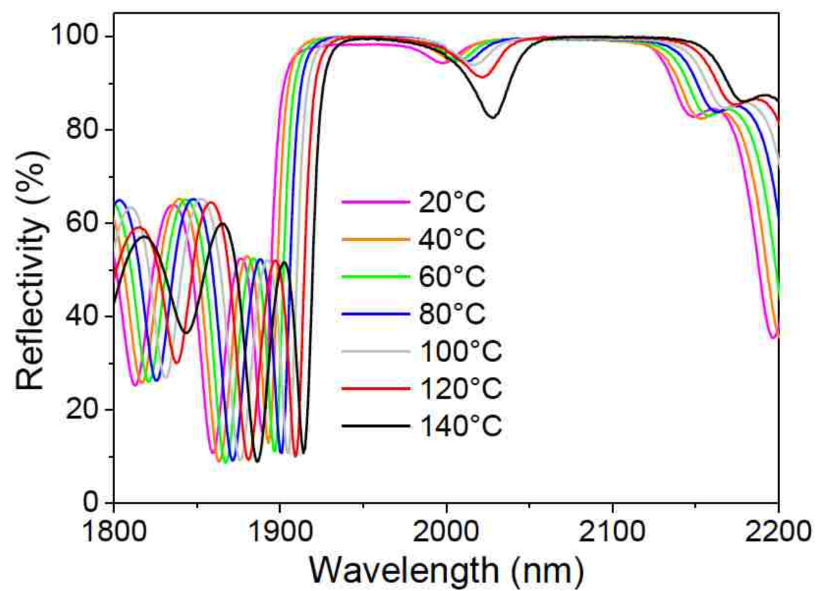

Figure 3.23: Temperature dependent reflectivity spectra from a VECSEL with growth rates not well calibrated, the gain-peak is much shorter than micro cavity resonance-peak

References

[1] Espen Selvig, *Molecular beam epitaxial growth and characterization of GaInAsSb/AlGaAsSb mid-infrared laser structures*, Ph.D. dissertation, Department of Electronics and Telecommunications, Norwegian University of Science and Technology, Trondhiem, 2004.

[2] M. A. Herman and H. Sitter, *Molecular beam epitaxy fundamentals and current status*: Springer-Verlag, 1989.

[3] S.H. Huang, G. Balakrishnan, A. Khoshakhlagh, A. Jallipalli, L.R. Dawson, D.L. Huffaker, *Strain relief by periodic misfit arrays for low defect density GaSb on GaAs*, Appl. Phys. Lett.,vol. 88, no.13, pp. 131911-1 -131911-3, Mar., 2006.

[4] A. Jallipalli, G. Balakrishnan, S.H. Huang, A. Khoshakhlagh, L.R. Dawson, D.L. Huffaker, *Atomistic modeling of strain distribution in selfassembled interfacial misfit dislocation (IMF) arrays in highly mismatched III-V semiconductor materials*, J. Cryst. Growth, vol. 303, no. 2, pp. 449-455, May 2007.

[5] T.J. Rotter, J. Tatebayashi, P. Senanayake, G. Balakrishnan, M. Rattunde, J. Wagner, J. Hader, J.V. Moloney, S.W. Koch, L.R. Dawson, D.L. Huffaker, *Continuous-Wave, Room-Temperature Operation of 2μm Sb-Based Optically-Pumped Vertical-External-Cavity Surface-Emitting Laser Monolithically Grown on GaAs Substrates*, Appl. Phys. Exp., vol. 2, no.11, pp. 112102-1112102- 3, Nov. 2009.

[6] A. Laurain et al., *Influence of non-radiative carrier losses on pulsed and continuous vecsel performance*, in [Vertical External Cavity Surface Emitting Lasers(VECSELs)], Tropper, A., ed., Proc. SPIE 8242, 82420S, 2012.

[7] A.M. Rocher, *Interfacial dislocations in the GaSb/GaAs (001) heterostructure*, Solid State Phenomena, vols. 19-20, pp. 563-572, Jan. 1991.

[8] W. Qian, M. Skowronski, R. Kaspi, *Dislocation density reduction in GaSb films grown on GaAs substrates by molecular beam epitaxy,* J. Electrochem. Soc., vol. 144, no. 4, pp. 1430-1434, Jan. 1997.

[9] M. Mehta, A. Jallipalli, J. Tatebayashi, M.N. Kutty, A. Albrecht, G. Balakrishnan, L.R. Dawson, D.L. Huffaker, *Room-Temperature Operation of Buffer-Free GaSbAlGaSb Quantum-Well Diode Lasers Grown on a GaAs Platform Emitting at 1.65 μm*, IEEE Photon. Technol. Lett., vol. 19, no. 20, pp. 1628-1630, Oct. 2007.

[10] O.G. Okhotnikov, *Semiconductor Disk Lasers:Physics and Technology*, Weinheim, Germany: Wiley-VCH Verlag GmbH & Co. KGaA, Apr. 2010.

[11] P Ahirwar, D Shima, TJ Rotter, SPR Clark, SJ Addamane, CP Hains, LR Dawson, G Balakrishnan, R Bedford, YY Lai, A Laurain, J Hader, JV Moloney, *TEM based analysis of III-Sb VECSELs on GaAs substrates for improved laser performance*, SPIE LASE, 86060E-86060E-12, 2013.

[12] P Ahirwar, T Rotter, D Shima, N Jahan, S Clark, S Addamane, G Balakrishnan, A Laurain, J Hader, Y Lai, J Moloney, I Suemune, R Bedford, *Growth and optimization of 2 μm InGaSb/AlGaSb quantum well based VECSELs on GaAs/AlGaAs DBRs*, IEEE-JSTQE, 2013.

Chapter 4

VECSEL: Lasing Characterization and Performance Analysis

The initial VECSEL wafer material characterization methods (Surface-PL, Edge-PL, Reflectivity and TDR) were discussed in Chapter 3. The gain-peak position is characterized by measuring room temperature PL spectra of active-region samples with a low-power He-Ne pump laser. The surface-PL spectrum from VECSEL samples is the result of QW emission being filtered by the gain chip sub-cavity. The peak in the surface-PL spectrum corresponds to subcavity resonance, but nonetheless the intensity of surface-PL is a good measure of QW optical quality. Each VECSEL sample is also checked for any surface defects using nomarski microscopy. Surface defects can result from group-III spitting (typically Ga) during MBE growth, insufficient oxide desorption from wafer surface, improper lattice matching for LM-VECSELs and from wafer handling during loading, unloading and wafer characterization. Although some initial attempts were done for lasing characterization of VECSEL samples grown at CHTM, due to lack of sufficient CW pump-power and a pulsed laser setup, the VECSEL samples were shipped to University of Arizona for laser characterization. A linear VECSEL cavity formed between DBR and an external output coupler is

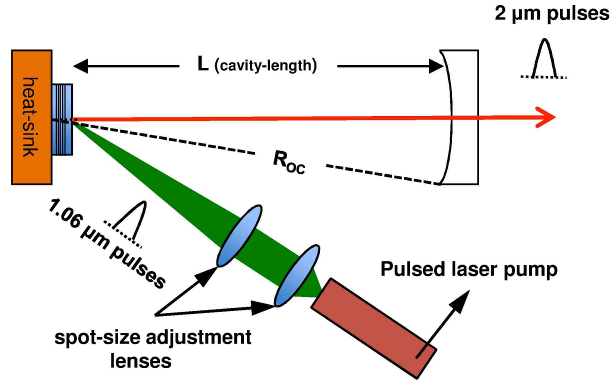

Figure 4.1: Schematic for optically pumped VECSEL operated in pulsed mode. (Figure taken from [1])

used for testing. The output coupler radius of curvature (R_{OC}) and cavity length (L) is chosen to achieve optimal matching between optical mode and pump-spot size. Results from pulsed and CW-lasing of LM-VECSEL and LMM-VECSEL are reported for combinations of several output coupler reflectivities (R) and pump-spot sizes (w_1). Furthermore a rate-equation based analysis and TEM-based analysis is done to compare the performance between LMM-VECSELs and LM-VECSELs.

4.1 LASER Characterization

4.1.1 Pulsed Lasing Characterization

Figure 4.1 shows the experimental setup for pulsed lasing characterization. The LMM-VECSEL samples were initially pumped optically by a pulsed source. This allows operation of the laser in a near sub-thermal regime without need for heat spreading elements. The pump-laser is a diode-pumped, Q-switched Nd:YAG laser

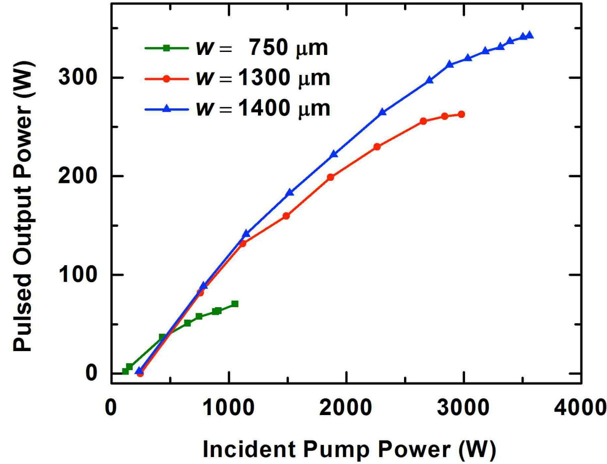

Figure 4.2: Peak output-power Vs peak pump power for the pulsed III-Sb VECSEL on GaAs substrate. (Figure taken from [1])

emitting at 1064nm. It is continuously pumped and repetitively Q-switched by an acousto-optic Q-switch. The repetition rate is 1kHz with a pulse width $\tau_{pulse} \sim$ 300ns , with available peak-powers up to 1.2 kW. The diameter of the pump-spot is adjusted by varying the distance between the VECSEL-chip and the pump-focusing lens. The laser beam was focused by means of a 12.5 cm focal length lens onto the LMM-VECSEL chip under test. The pump beam is nominally TEM_{00}. A linear cavity of length Lc = 70 mm is used, giving a fundamental mode radius of 178 μm at the lasing wavelength of 2μm. Figure 4.2 shows the pulsed peak output power versus peak pump power for a LMM-VECSEL. The threshold incident pump power density is calculated to be 17.44 kW/cm^2. As shown in Figure 4.2, the maximum OPSL power was observed when the beam diameter is 1400 μm, however the output-beam has multiple modes. The peak output power from this device has been reported as high as 340 W (with a 143-ns pulsewidth when the peak pump power was 5.5 kW with 160-ns pulsewidth)[2]. With a further increase in pump-power, a maximum output peak power of 378W is observed with approximately 6 kW pump power,

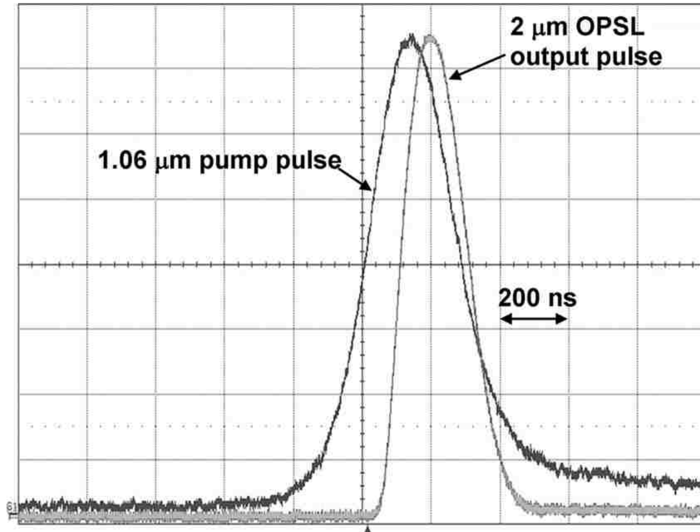

Figure 4.3: Time resolved pump and 2μm VECSEL pulse shapes. (Figure taken from [2])

however the VECSEL chip was damaged.

Figure 4.3 shows the temporal pulse shape of the pump-laser and the 2 μm LMM-VECSEL output under typical operating conditions. The pump-pulse is measured with a fast silicon photodiode while the VECSEL emission is measured with an extended InGaAs detector. The pump pulse is Gaussian shaped temporally. The peak power is calculated by measuring the average power and dividing by the duty cycle of the laser. The time averaged emission spectra of the VECSEL is measured using an infrared spectrometer (AvaSpec-NIR256-2.5, by Avantes Inc.). The spectrum consists of a single peak at 1995 nm.

4.1.2 CW Lasing Characterization

CW-lasing characterization is done using an intra-cavity heat spreader (transparent diamond or silicon carbide, SiC) for thermal dissipation, the setup is shown schematically in Figure 4.4. The VECSEL sample substrate is thinned to $\sim$ 100 μm. The

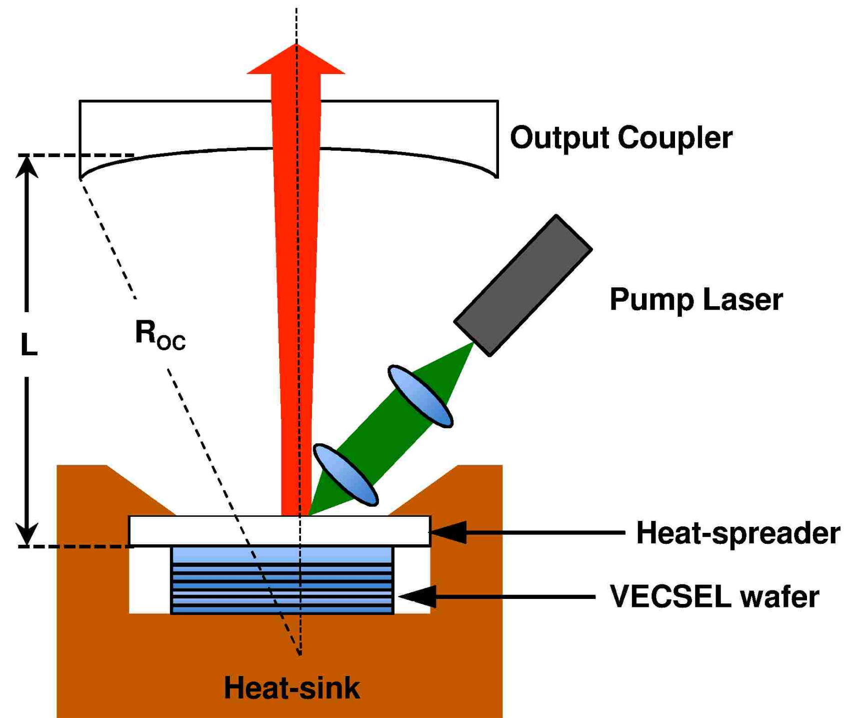

Figure 4.4: Schematic for optically pumped VECSEL operated in CW mode.(Figure taken from [1])

substrate is metallized with Ti-Pt-Au and then thin Indium foil is used to bond the sample to a copper heat-sink. In order to dissipate heat generated in the active region most efficiently, a transparent heat-spreader is attached to the epi-side of the sample by means of capillary bonding. The epi-surface must be defect free and quality is very crucial to form a good capillary bond.

In Chapter 3, Section 3.2.4, two types of VECSEL designs were discussed;

- where the quantum wells as well as all refractive index steps (except for the IMF) are located at field antinodes, sample R8-130 is based on this structure.
- and another design, where only the quantum wells are located at field antinodes

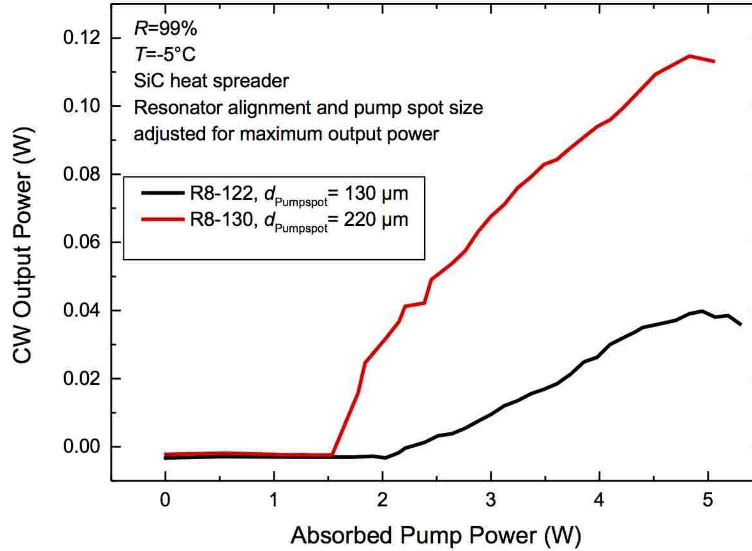

Figure 4.5: Comparison of the two VECSELs R8-130 and R8-122 operated with a SiC heat spreader and an output coupler with 99% reflectance at -5 °C.

and all other refractive index steps and IMF are located at field nodes. (Sample R8-122 is based on this design)

The structural difference is outlined in Figure 3.18. Figure 4.5 compares the lasing performance of two VECSEL designs (R8-122, R8-130). For both VECSEL samples a SiC heatspreader is capillary mounted on wafer surface for heat extraction. A 99% output coupler is used for lasing characterization, while the spot-size is adjusted for maximum output power. The placement of refractive index steps at nodes causes poor reflectance and hence lead to suboptimal performance for sample R8-122.

Figure 4.6 shows the L-L chracteristics for LMM-VECSEL (R8-130) for heat-sink temperatures in the range of -5 to 20 °C. A 980nm fiber coupled diode laser is used for photopumping of this VECSEL device. The device is pumped at an incident angle of

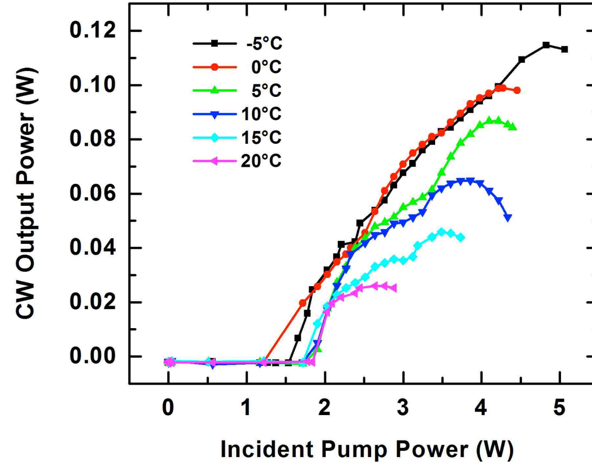

Figure 4.6: Output power versus absorbed pump power of the VECSEL R8-130 operated with a SiC heat spreader and an output coupler with 99% reflectance at different operating temperatures. The maximum output power achieved is 120 mW CW at 130 μm pump spot diameter. The maximum temperature for CW operation in this arrangement is 20°C, the pump threshold at this temperature is 13.9 kW cm^{-2}. (Figure taken from [1])

30° with a pump-spot size of $w_1 = 130\mu$m. The threshold pump power density (P_{th}) is calculated to be 13.9 kW/cm^2 for the laser operating at 20 °C.[3] The maximum CW output power is observed to be $\sim$ 120 mW at a heat sink temperature of -5 °C.

Figure 4.7 shows the L-L characteristics for the LM-VECSEL for an output coupler with R ~96% , and pump-spot size $\sim$ 400 μm at a hest sink temperature of 5 °C. A 1064nm-YAG laser is used for photopumping of this device from heat spreader side. A single crystal transparent diamond is capillary bonded to the epi-side is used as a heat spreader in this case. The threshold pump power density (P_{th}) is calculated to be 1.19kW/cm^2 for laser device operating CW at heat sink temperature of 5 °C for a pump-spot size of 400 μm. The maximum CW output power is observed to be $\sim$ 3W.

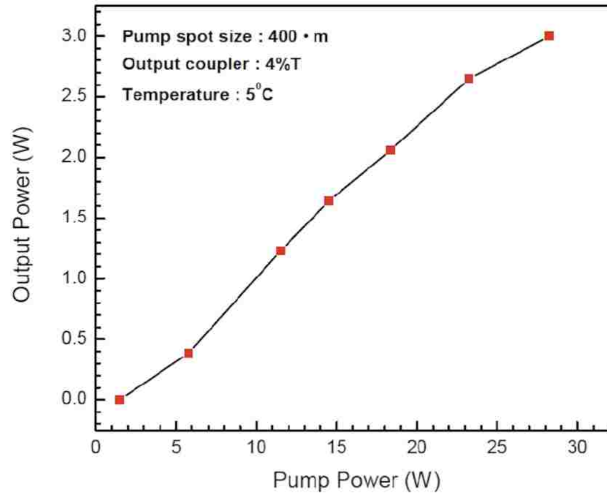

Figure 4.7: Output power versus absorbed pump power of the LM-VECSEL operated with a diamond heat spreader and an output coupler with 96% reflectance. The maximum output power achieved is 2.95W CW at 400 μm pump spot diameter. (Figure taken from [1])

4.2 Effects of mismatched epitaxy on VECSEL performance

The two types of VECSELs discussed in this dissertation have very similar structures, however the lattice-matched VECSEL outperform the lattice-mismatched VECSELs. This can be seen in Table 4.1 which shows the key metrics for two types of VECSELs. The mismatched VECSELs threshold pump power density is with 13.9 kW/cm^2 much higher than 1.19 kW/cm^2 for the lattice-matched VECSEL. Furthermore there is also a significant decrease in the wall-plug efficiency and the maximum CW output power obtained from the lattice mismatched laser grown on a GaAs/AlGaAs DBR. It can be speculated that the deterioration in the performance of the VECSEL when grown mismatched on GaAs compared to when it is grown lattice matched on GaSb can be attributed to the presence of threading dislocations in the active region when it

Table 4.1: Key lasing performance metrics for a lattice-mismatched III-Sb VECSEL on GaAs/AlGaAs DBR versus those for a lattice-matched VECSEL grown on GaSb/AlAsSb DBR.

Device	$\eta_d(\%)$		$P_{th}(kW/cm^2)$		$P_{max-CW}(W)$
	Pulsed	CW	Pulsed	CW	
LMM-VECSEL	10.3	3.5	22	13.9	0.12
LM-VECSEL	15.2	14.1	1.19	1.2	2.95

is grown on the GaAs/AlGaAs DBR.

4.2.1 Rate equation based performance analysis of VECSELs

The two devices (LMM-VECSEL and LM-VECSEL) have a similar active region, consisting of $Ga_{0.8}In_{0.2}Sb$ MQW gain-region separated by pump-absorbing $Al_{0.25}Ga_{0.75}Sb$ barriers and a top/bottom AlSb clad. The growth conditions for both devices were optimized and epitaxial growth was done in the same MBE reactor. The carrier loss equation in VECSEL structures can be modeled as follows;

$$R_{loss} = R_{Defect} + R_{SE} + R_{Auger} + R_{remaining}\ , \tag{4.1}$$

Where R_{loss}: carrier loss rate, R_{Defect}: carrier loss rate due to carrier recombination via defect states, R_{SE}: carrier loss rate due to spontaneous emission processes , R_{Auger}: carrier losses due to Auger recombination processes , $R_{remaining}$: carrier loss due to carriers not captured by wells or tunneled carriers not re-captured in other wells. The carrier density dependencies in equation 4.1 are derived using crude approximations for underlying physical processes[4]. The linear dependence of R_{Defect} is based on the assumption that the defect states energy levels are close to the con-

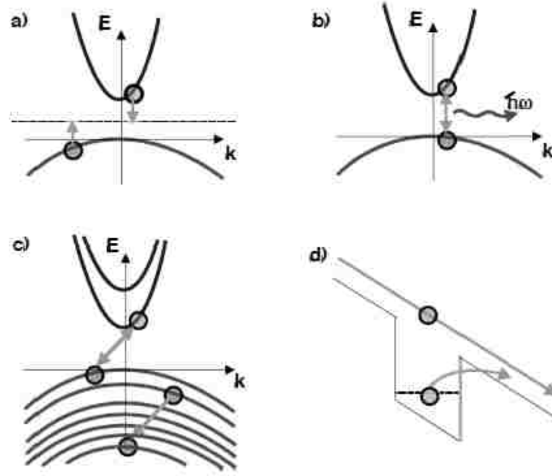

Figure 4.8: Schematic representation of carrier recombination processes in semiconductor lasers (a) Recombination via defect states (b) Spontaneous recombination processes (c) Auger recombination processes (d) carier non-capture and escape processes (Figure taken from [4])

duction band edge. In this, the electrons get trapped quickly into these defect states and the recombination rate depends on how long it takes for a hole to be captured into the defect states. Also, assuming that the transition probability is same for all holes and defect states, the total recombination rate is equal to the capture rate for one hole times the number of holes and hence R_{Defect} scales linearly with carrier density (N). The process is schematically shown in Figure 4.8(a). In a spontaneous emission process (R_{SE}) electrons and holes have to be present at the same time, (Figure 4.8(b)) thus N^2 dependance follows intuitively. The N^3 dependance for Auger Processes (Figure 4.8(c)) is due to the fact that three carriers need to be present at the same time, two carriers that recombine and one carrier takes up the released energy. A schematic illustration for carrier escape and non-capture processes are shown in Figure 4.8(d).

A widely accepted model to represent the rate of carrier loss in semiconductors is

also known as 'ABC' model (Equation (4.2) models VECSEL carrier-loss rate (R_{loss}) with 'ABC' parameters);

$$R_{loss} = AN + BN^2 + CN^3 + R_{remaining} = N/\tau\,, \tag{4.2}$$

where τ is the carrier lifetime under low carrier concentration (no stimulated emission) and A, B, C are constant coefficients. For the VECSEL structures discussed in this dissertation typically $R_{remaining} \sim 0$ (as most of the carriers generated in the barrier region have high probability of being captured in the QW and carrier capturing is also enhanced by clad layers). However the 'ABC' empirical model is not adequate to model the carrier losses at high carrier density and high temperature (typical operating conditions of a high power VECSEL). At such high carrier densities the distribution of carriers does not follow the Maxwell-Boltzman distributions, instead it can be approximated by step-like Fermi-distributions that are 1 for energies below the chemical potential and zero above[4]. Thus at carrier densities near and beyond the transparency, a strong deviation from 'A,B,C' power law is observed[5]. To account for the change of loss rate with temperature, the temperature dependency for B and C coefficients also needs to be included in the model[6]. A fully microscopic many-body approach used for computation of losses has shown a better agreement between experimental and theoretical data[7, 8]. The carrier loss equation can be represented as follows;

$$R_{loss} = AN + R_{SE}(N,T) + R_{Auger}(N,T) = N/\tau_d + BN^2 + CN^3 = N/\tau\,, \tag{4.3}$$

Here R_{SE}, R_{Auger} are function of carrier density (N) and operating temperature of the device (T) and τ_d is the inverse of the Shockley-Read-Hall coefficient "A".

For evaluating the radiative and non-radiative losses in the VECSEL structures, one of the methods is to measure the internal quantum efficiency at different pump

power density. The internal quantum efficiency of the gain structure is defined as the ratio between carrier recombining through spontaneous recombination to the total number of absorbed pump photons: $\eta_i = R_{SE}/R_{loss}$. η_i can be inferred experimentally by measuring the number of photons per unit time, recorded by a photodetector positioned normal to the VECSEL surface[9]. The number of photons incident per unit time on a photodetector with a square aperture, of area a, distance D and positioned normal to VECSEL surface is given by the following expression;

$$N_{PD} = \frac{aN_{QW}}{4\pi n^2 D^2} \int f(\lambda)\mu(\lambda)T(\lambda)d\lambda\,, \tag{4.4}$$

Here, n is the refractive index of the layer within which the well is embedded, also it is assumed quantum wells within the active region emit as point source isotropically at the overall rate $\mathrm{N_{QW}s^{-1}}$, or at $\mathrm{N_{QW}}f(\lambda)/4\pi s^{-1}sr^{-1}\mu m^{-1}$, where $f(\lambda)$ is a normalised spectral distribution function for which $\int f(\lambda)d\lambda = 1$. $\mu(\lambda)$ is the microcavity enhancement factor. The radiative quantum efficiency is related to $\mathrm{N_{QW}}$ by $\eta_i = (N_{QW}/N_{absorbed-photons})$.

At very low carrier densities, the non-radiative losses in a VECSEL structure are dominated by defect assisted recombinations. Thus this method is particularly useful to estimate these losses, which strongly depend on the epitaxial growth conditions of the VECSEL samples. The experimental and theoretical values of quantum efficiencies are shown in Figure 4.9 for both LMM and LM-VECSEL structures[5]. From comparison of theoretical with experimental results, the value of defect recombination coefficient is estimated to be $\tau_d = 2.6$ ns for LMM-VECSEL. The τ_d for the LM-VECSEL structure is determined to be 16 ns. The low value of τ_d for LMM-VECSEL can be attributed to the presence of dislocations in the active region. These defects act as non-radiative recombination centers and can also effect the properties such as thermal conductivity of the material[9]. The lower value of τ_d (higher losses in the device) increase the threshold power density of the device. High losses in the device also reduce the maximum CW output power which can be obtained from the

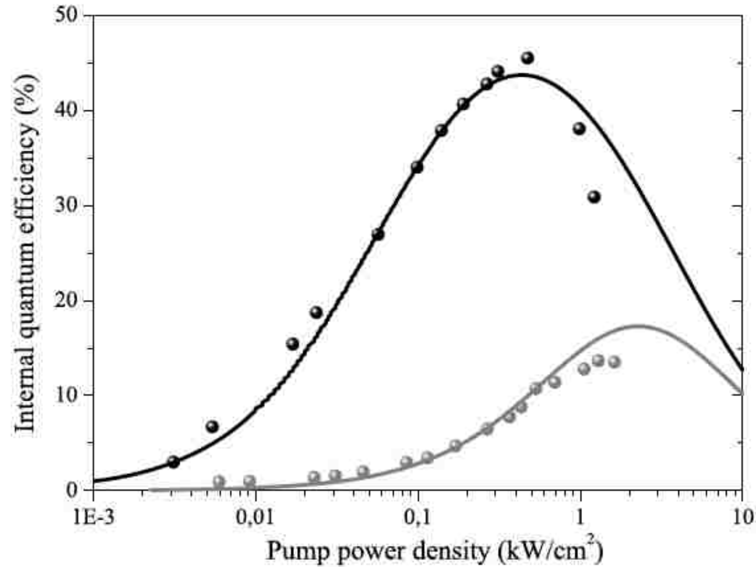

Figure 4.9: Internal quantum efficiency versus incident pump power density. Black circles: experimental η_i for LM-VECSEL. Gray-circles: Experimental η_i for LMM-VECSEL. Black-line: theory assuming a defect recombination coefficient A^{-1}= 16ns. Gray-line: theory assuming a defect recombination coefficient A^{-1}= 2.6ns. (Figure taken from [5])

VECSEL chip.

4.2.2 TEM based analysis of threading dislocations in VECSELs

The cause of the sub-optimal performance of the LMM-VECSEL is investigated in this section. From experimental and theoretical data, the low value of τ_d points to a high number of defects within the active region. For a III-Sb device on GaAs the mismatch strain is relieved at the (GaSb/GaAs) interface through misfit-dislocations. Threading dislocations (TD) are associated with misfit dislocations and can propagate in the mismatched epitaxial layer. Such dislocations are linear defects with disrupted interatomic bonding. The core of dislocation has dangling bonds sur-

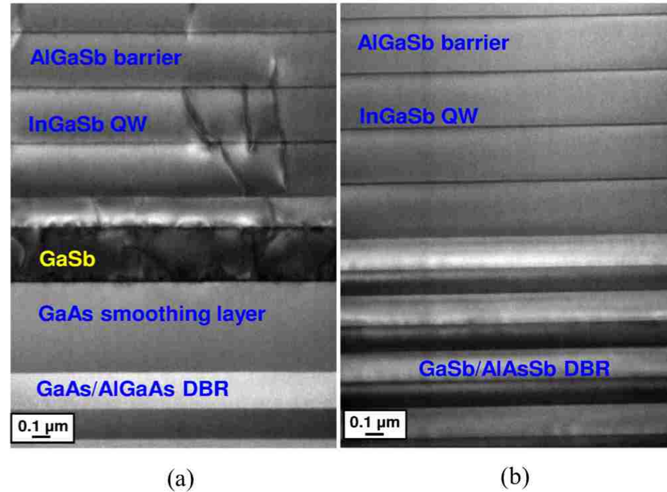

Figure 4.10: TEM comparison of LMM-VECSEL and LM-VECSEL. (a) shows the lattice mismatched structure with extensive threading dislocations in the active region and (b) shows the complete absence of threading dislocations in the lattice matched structure. (Figure taken from [1])

rounded by regions with distorted atomic bonds. The investigation of the threading dislocation density (TDD) in the III-Sb VECSELs involves cross section transmission electron microscopy analysis of both the VECSEL structures. These VECSELs are cross-sectioned with a focused ion beam (FIB) lift out using a FEI Helios 450 DIB system. The TEM images were taken using an FEI Tecnai F20 equipped with HAADF STEM detector. For the initial TEM/STEM imaging the samples were ∼150nm thick near the top of the active region and ∼ 250nm thick near the active region /DBR interface.

Figure 4.10 shows high resolution cross-sectional TEM images comparing the two VECSELs. In case of a lattice-mismatched VECSEL the strain between GaSb/GaAs is relieved at the interface by forming misfit dislocations at the interface. The IMF interface may have breaks and discontinuities when grown on GaAs/AlGaAs DBR compared to the IMF interface on GaAs substrates. This irregularly formed IMF

interface leads to threading dislocations at these discontinuities as can be seen in Figure 4.10(a). These threading dislocations can reach into the active region and are the source for the non-radiative recombination and the reduced value of τ_d. The high resolution cross-sectional TEM image of lattice-matched VECSEL (Figure 4.10(b)) shows no threading dislocations in the III-Sb active region. It is evident from the XTEM image of the III-Sb active region that the lattice-mismatched VECSEL contains a significant density of dislocations. The presence of dislocations within the carriers diffusion length leads to reduced of carrier lifetime[10]. The carrier lifetime is related to the dislocation density N_D by the following formula

$$\frac{1}{\tau_d} = \frac{\pi \mu k_B T N_D}{4q}, \tag{4.5}$$

where τ_d is the carrier lifetime associated with recombination assisted by dislocations, μ is the mobility of minority carriers, q is the electronic charge. The overall carrier lifetime τ is then,

$$\frac{1}{\tau} = \frac{1}{\tau_0} + \frac{1}{\tau_d}, \tag{4.6}$$

where τ_0 is the carrier lifetime in dislocation free material. The carrier lifetime in a III-Sb VECSEL grown on GaSb/AlAsSb DBR is closer to τ_0, as it is almost free of dislocations as can be seen in the high resolution TEM image.

It can be seen in equation (4.5), that the carrier lifetime is inversely proportional to the TDD (N_D) in a material. In a TEM image one can measure the total projected length of dislocation lines l', the dislocation density can then be estimated using the following formula,[11]

$$N_D = \frac{4}{\pi} \frac{l'}{At}, \tag{4.7}$$

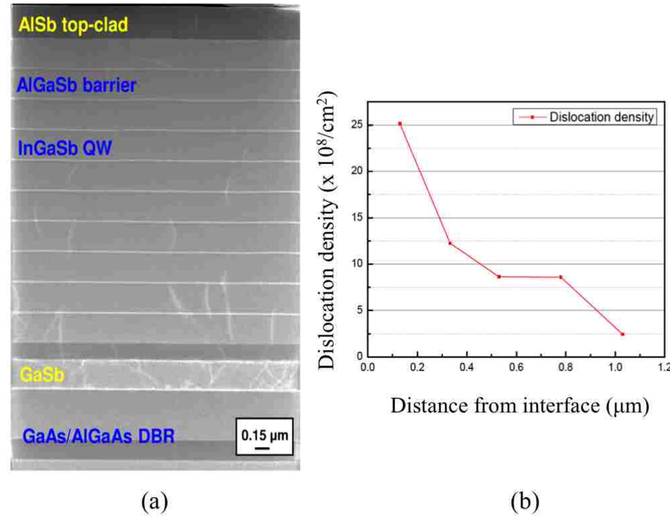

Figure 4.11: (a) STEM image of LMM III-Sb VECSEL on GaAs/AlGaAs DBR showing the source of the threading dislocations at the IMF array (b) subsequent reduction in the density as a function of distance from the mismatched interface. (Figure taken from [1])

where t is the thickness of the TEM sample , A is the area over which the projected length l is estimated. The dislocation density N_D as a function of the distance from the GaSb/GaAs interface for VECSEL structures shown in Figure 4.11(a) is determined using 4.7. The dislocation density reduces from $\sim 10^9 cm^{-2}$ to about $\sim 10^8 cm^{-2}$ at a distance of about ~ 1.1 μm from the interface (shown in Figure 4.11(b)). Thus it is evident from the relationship between carrier lifetime and dislocation density, higher TDD is detrimental to performance of a VECSEL device[5]. The high P_{th} (threshold pump power density), low CW output power and poor slope efficiency for III-Sb VECSEL grown on a GaAs substrate can be linked to high TDD in active regions of these devices.

4.2.3 Effect of Threading Dislocations on Thermal Conductivity

For an optically pumped semiconductor laser with active region gain at λ_{QW} photo pumped by a pump wavelength λ_{pump}, the carriers are generated with extra energy $(hc/\lambda_{pump} - hc/\lambda_{QW})$, which must be dissipated for every emitted photon. The thermal loading of a VECSEL device is greatly enhanced by presence of non-radiative recombination centers or defects and Auger recombination at high pump intensities[5, 12, 9]. The thermal sensitivity of QW gain medium is much greater than that of the DBR. An increased temperature in the active region spreads out the thermal distribution of carriers and can also lead to the escape of confined carrier if the confinement potential is not high enough. The thermal impedance of the gain region of the VECSEL chip is hence related to thermal conductivity of the gain medium and spatial temperature distribution[9]. The temperature distribution can be expressed by following expression (assuming uniform heat input over circular disc of radii $w_o/2$ on slab of thickness d)

$$\Delta T_{max} = \frac{P_{thermal}}{k\pi w_0^2}\left[w_0 + 2d - \sqrt{w_0^2 + 4d^2}\right] , \tag{4.8}$$

where k is thermal conductivity of gain region or DBR region.

The amount of thermal power resulting from photo pumping of the VECSEL devices with incident pump power $P_{incident}$ is given by following expression;

$$P_{thermal} = P_{incident}T_r\left[A_b\left(1 - \eta_i\frac{\lambda_{pump}}{\lambda_{QW}}\right) + (A_b - 1)\left(1 - \eta_b\frac{\lambda_{pump}}{\lambda_{QW}}\right)\right] , \tag{4.9}$$

where the first term in equation (4.9), accounts for the heat generated in the RPG region, and the second term is for pump power not absorbed in RPG region and converted to heat in DBR, η_i and η_b are the radiative efficiencies of the RPG

and Bragg regions respectively[5]. For 2 μm VECSEL devices pumped with $\lambda_{pump} =$ 908nm or 1060 nm , the first term is the dominant thermal source (heat generated in RPG region). Therefore the ΔT_{max} is related to the thermal power generated in RPG region and inversely related to thermal conductivity of the RPG region i.e. k_{RPG} as follows;

$$\Delta T_{max} \propto \frac{1}{k_{RPG}} P_{thermal} \,, \tag{4.10}$$

The dominant contribution to thermal conductivity of the semiconductor comes from acoustic phonons[13] hence the contribution of electronic thermal conductivity can be neglected. Thus the lattice thermal conductivity of RPG-gain region can be expressed as;

$$k_{RPG} = \left(\frac{2\pi k_B}{h}\right)^3 \frac{k_B}{2\pi^2 \nu} T^3 \int_0^{\Theta_D/T} \frac{\tau_c x^4 e^x}{(e^x - 1)^2} dx \,, \tag{4.11}$$

where k_B is the Boltzmanns constant , h is the Plank constant, T is the absolute temperature, ν is the average sound velocity, Θ_D is the Debye temperature , τ_c is the combined phonon relaxation time , ω is phonon frequency and $x = h\omega/2\pi k_B T$.

τ_c is the relaxation time between phonon scattering, for pure materials $1/\tau_c =$ $1/\tau_U$, where τ_U is the relaxation time related to intrinsic thermal conductivity of the semiconductor. However in presence of point defects and dislocations the relaxation time for phonons can be expressed as follows[13, 14]

$$1/\tau_c = 1/\tau_U + 1/\tau_P + 1/\tau_D \,, \tag{4.12}$$

where $1/\tau_P$ is the phonon relaxation rate on point defects, $1/\tau_D$ is the phonon relaxation on dislocations.

Now for both the VECSEL structures $1/\tau_U$ & $1/\tau_P$ are comparable as the two samples have almost similar active-region. The only noticeable difference to $1/\tau_c$ can be from dislocations in the semiconductor material (RPG region). Phonons scatter

on dislocations by two mechanisms , first one is by elastic field strain of dislocation lines , second mechanism is scattering at core of dislocations. This phonon scattering at core of dislocations ($1/\tau_{DC}$) is given by following expression;

$$\frac{1}{\tau_{DC}} = \eta N_D \frac{V_0^{4/3}}{\nu^2} \omega^3 , \tag{4.13}$$

where N_D is the density of the dislocation lines of all types (assuming all dislocations types originate from a dislocation core) , η is the weight factor accounting for orientation of dislocations with respect to temperature gradient,[13] V_o is the unit cell volume for zinc blende type crystal, ν is the sound velocity and ω is the phonon frequency. The elastic field of edge ($1/\tau_E$) and screw dislocations ($1/\tau_S$) and mixed dislocations ($1/\tau_M$) is related to N_D and characteristic Burgers vector for dislocation type as shown in following relation.

$$1/\tau_E, 1/\tau_S, 1/\tau_M \propto f(\eta, N_D, b_S, b_E, b_M) , \tag{4.14}$$

$b_{S,E}$; screw and edge burger vectors in Zinc Blende crystal. $b_M = b_S + b_E$ is the burger vector for mixed dislocation. Phonon relaxation is assumed to be independent process due to the dislocations , thus the combined effect of all dislocation types can be expressed as,

$$\frac{1}{\tau_D} = \frac{1}{\tau_{DC}} + \frac{1}{\tau_S} + \frac{1}{\tau_E} + \frac{1}{\tau_M} , \tag{4.15}$$

This $1/\tau_D$ can be put in equation (4.12) and equation (4.11) to estimate k_{RPG} . It can be inferred from this relation that $k_{RPG} \propto 1/N_D$. It has been shown[15] the thermal conductivity for GaN films can be limited by dislocations when their density is high. Thus thermal loading of the VECSEL device due to dislocation enhanced scattering and auger processes and quantum defect can overheat the device. This thermal loading is more pronounced in III-Sb VECSEL structures grown on GaAs

substrates, due to high TDD $\sim 10^9 cm^{-2}$, it can even prevent these devices from turning on. However for pulsed operation, the defect related losses are not as crucial as for CW operation of the devices. For a relatively short pulse ($\tau_{pulse} < 300ns$) , the devices can be photo pumped with high pump power density without overheating them.

4.3 Strategies for Threading Dislocation reduction

The detrimental effect of the high TDD in the LMM-VECSELs active region requires strategies for either reducing these dislocations or bending the dislocations before they can reach the active regions. One option is to improve the IMF interface when the GaSb is grown on GaAs/AlGaAs DBR and the second approach is to move the IMF interface further away from the active region.

4.3.1 Optimization of the IMF interface using time-resolved PL measurements.

A comprehensive study on the effect and influence of misfit dislocation arrays on the optical and carrier thermo-dynamical properties of semiconductor hetero-structures has been done by Nahid A Jahan et al.[16]. The optical properties such as luminescence spectra, quantum efficiency and recombination lifetime are measured for $GaSb/Al_{0.5}Ga_{0.5}Sb$ quantum well samples grown on (001) GaAs substrates. The sample structures are shown in Figure 4.12. Sample 4.12(a) was grown with IMF-growth mode, while 4.12(b) is grown directly on GaAs without formation of IMF at the interface. The temperature-dependent time-integrated PL measurements on the

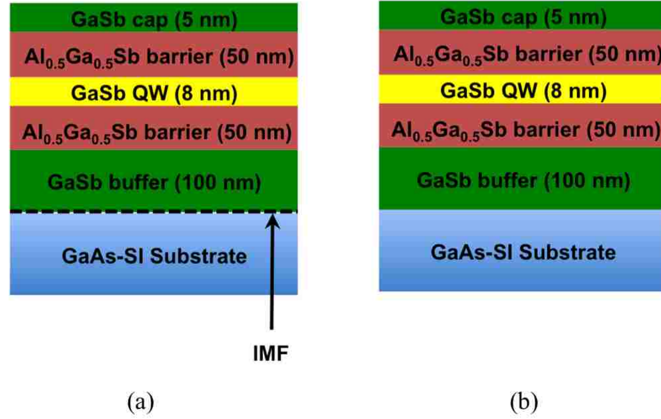

Figure 4.12: (a) Schematic of III-Sb PL Test sample grown epitaxially on GaAs with IMF (b) Schematic of III-Sb PL Test sample grown epitaxially on GaAs without IMF.

two QW samples are performed under the low excitation power of 6 W/cm^2. The spectrally integrated PL intensity is given by following Arrhenius equation;

$$I(T) = \frac{I_0}{1 + Bexp(-E_a/k_B T)}, \tag{4.16}$$

where I_0 is the integrated PL intensity at 0K, E_a is the thermal activation energy, k_B is the Boltzman constant, and T is the sample temperature in Kelvin. B is the dimensionless coefficient (ratio of carrier capture time to carrier escape time for non-radiative recombination process)[16]. The activation energies for IMF and non-IMF QWs are estimated to be 16 ± 3 meV and 10 ± 2 meV respectively, by fitting experimental data to the equation (4.16).

The carrier-dynamics and thermally activated escape processes in the QW structures are investigated by doing time-resolved PL measurements on the samples. These measurements are performed as a function of excitation power and sample

temperature. The experimentally measured transient PL intensity as a function of excitation power is fitted with a double exponential function, $I(t) = I_{dark} + A_1 exp(-t/\tau_1) + A_2 exp(-t/\tau_2)$, where I_{dark} is the dark count without pulsed laser excitation signal. τ_1 and τ_2 are the time-constants for ground-state decay-time and excited-state decay-time respectively. The ground-state decay-time (τ_1) for IMF-QW is estimated to be $\sim$ 1ns for an excitation power in range of 30 W/cm^2 to 3 kW/cm^2. For a similar excitation power range the ground-state decay-time (τ_1) for QW-no-IMF is around 1.5ns. The excited-state decay-time (τ_2) increases from 220ps to 350ps for an increase of excitation power from 30 W/cm^2 to 3 kW/cm^2 for a IMF-QW. An increase in the value of τ_2 indicates band-filling effect. As the number of carriers occupying excited-states increases with excitation power, it slows down of the energy relaxation rate of carriers occupying excited states. The excited-state decay time in case of non-IMF QW stays at a constant value of $\sim$ 250ps with an increase of excitation-power in similar range. This indicates the band-filling effect is quenched in case of a non-IMF QW. This quenching can be caused due to presence of additional non-radiative recombination processes or carrier-leakage paths in non-IMF QW samples. A higher threading-dislocation (TD) density is typically observed in samples grown without IMF interface when compared to samples grown using IMF technique. A high TDD can thus cause quenching of the band-filling effect of excited carriers.

The temperature-dependent time-resolved PL measurements are done for both IMF-QW and no-IMF-QW at a constant excitation power $\sim 30W/cm^2$. The temperature dependence of ground-state decay time constant is fitted using following equation;

$$\tau(T) = \frac{\tau_d}{1 + (\tau_d/\tau_e)\, exp\left(-E_a/k_B T\right)}\,, \tag{4.17}$$

where T is the temperature in K , k_B is the Boltzman constant, τ_d is the recombination lifetime at the lower temperature limit, E_a is the activation energy, and τ_e

is the carrier-escape time from QW to the barriers. The fitting of the experimental data results for the two types of QW is listed in Table (4.2) .

Table 4.2: Experimental Fitting Data results for determining ground-state decay time constant.

QW	Activation Energy (E_a)	τ_d	τ_e
IMF	16 ± 3meV	1006 ± 21ps	53 ± 8ps
No-IMF	10 ± 2meV	1606 ± 20ps	10 ± 3.7ps

It is clear from the time-resolved PL measurements that the PL quenching activation energy for a non-IMF-QW is smaller than for an IMF-QW. The carrier escape time from QW ⇒ barrier is also shorter for non-IMF-QW when compared to a IMF-QW sample. This suggests the non-IMF-QW have additional carrier-escape paths. These carrier-escape paths can be related to higher threading-dislocation densities in these samples. Thus threading dislocations play an important role in determining the carrier lifetime of excited carriers, and could also lead to PL-quenching in active regions with high threading dislocation densities. Hence time-resolved PL measurement is an effective technique to determine the quality of IMF interface and can be used as an method to optimize performance of III-Sb active regions grown on GaAs/AlGaAs DBRs.

4.3.2 Placement of III-Sb active region away from the IMF Interface.

The presence of threading dislocation in the active region of the III-Sb VECSEL devices is detrimental for the laser performance as it degrades both optical and thermal properties. A reduction in TDD in the GaSb epi-layer away from the IMF-interface can be observed in Figure 4.11(b). The TDD at a distance of about ∼ 1.1μm from the interface is about 2 x $10^8 cm^{-2}$ which is almost ∼ 10 times lower

than the TDD density near the IMF interface. The LMM-VECSEL discussed till now, has been grown on a MOCVD grown GaAs/AlGaAs DBR. The formation of a coherently linked IMF interface on rough DBR surface is challenging. Figure 4.13 shows STEM image of a GaSb/AlAsSb DBR epitaxially grown a GaAs substrate. This GaSb/AlAsSb DBR on GaAs substrate is typically 5-6 μm thick. The top layers of the DBR are free of any threading dislocations, as can be seen in Figure 4.13. Thus III-Sb active-regions grown on such DBR should be typically free of threading dislocations and can have performance similar to III-Sb VECSELs grown on GaSb substrates.

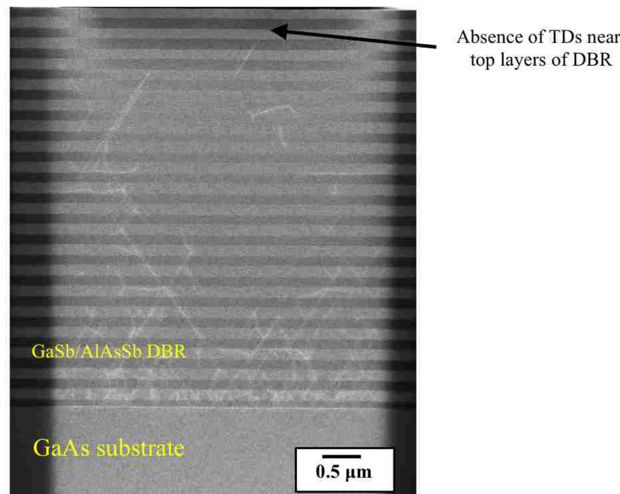

Figure 4.13: STEM image of GaSb/AlAsSb DBR on GaAs substrate (subsequent reduction in the threading dislocation density away from the mismatched interface can be seen). (Figure taken from [17])

References

[1] P Ahirwar, T Rotter, D Shima, N Jahan, S Clark, S Addamane, G Balakrishnan, A Laurain, J Hader, Y Lai, J Moloney, I Suemune, R Bedford, *Growth and optimization of 2 μm InGaSb/AlGaSb quantum well based VECSELs on GaAs/AlGaAs DBRs*, IEEE-JSTQE, 2013.

[2] Y.Y. Lai, J.M. Yarborough, Y. Kaneda, J. Hader, J.V. Moloney, T.J. Rotter, G. Balakrishnan, C. Hains, S.W. Koch, *340-W Peak Power From a GaSb 2-?m Optically Pumped Semiconductor Laser (OPSL) Grown Mismatched on GaAs*, IEEE Photon. Technol. Lett., vol. 22, no. 16, pp. 1253-1255, Aug. 2010.

[3] T.J. Rotter, J. Tatebayashi, P. Senanayake, G. Balakrishnan, M. Rattunde, J. Wagner, J. Hader, J.V. Moloney, S.W. Koch, L.R. Dawson, D.L. Huffaker, *Continuous-Wave, Room-Temperature Operation of 2-?m Sb-Based Optically-Pumped Vertical-External-Cavity Surface-Emitting Laser Monolithically Grown on GaAs Substrates*, Appl. Phys. Exp., vol. 2, no.11, pp. 112102-1112102- 3, Nov. 2009.

[4] J. Hader, J.V. Moloney, S.W. Koch, L. Fan, M. Fallahi, *Carrier Recombination in Semiconductor Lasers: Beyond the ABC*, Numerical Simulation of Semiconductor Optoelectronic Devices, 2006. NUSOD '06. International Conference on, pp. 39-40.

[5] A. Laurain et al., *Influence of non-radiative carrier losses on pulsed and continuous vecsel performance*, in [Vertical External Cavity Surface Emitting Lasers(VECSELs)], Tropper, A., ed., Proc. SPIE 8242, 82420S (2012).

[6] OReilly, E. P. and Silver, M., *Temperature sensitivity and high temperature operation of long wavelength semiconductor lasers*, Appl. Phys. Lett. 63(24), 33183320 (1993).

[7] J. Hader, G. Hardesty, T.-L. Wang, M.J. Yarborough, Y. Kaneda, J.V. Moloney, B. Kunert, W. Stolz, S.W. Koch, *Predictive microscopic modeling of VECSELs*, IEEE J. Quantum Electron., vol. 46, no. 5, pp. 810817, May 2010.

[8] J. Hader, J.V. Moloney, S. Koch, *Microscopic evaluation of spontaneous emission- and Auger-processes in semiconductor lasers*, IEEE J. Quantum Electron.,vol. 41, no. 10, pp. 12171226, Oct. 2005

[9] A.C. Tropper and S. Hoogland, *Extended cavity surface-emitting semiconductor lasers*, Prog. Quantum Electron., vol. 30, no. 1, pp. 1-43, Jan. 2006.

[10] Ayers, J., *Heteroepitaxy of Semiconductors: Theory, Growth and Characterization*, CRC Press, Boca Raton (2007).

[11] Butler, T. W., *On the determination of dislocation densities*, tech. rep., USNA Engg. Dept. (1969).

[12] O.G. Okhotnikov, *Semiconductor Disk Lasers:Physics and Technology*, Weinheim, Germany: Wiley-VCH Verlag GmbH & Co. KGaA, Apr. 2010.

[13] Kotchetkov, D., Zou, J., Balandin, A. A., Florescu, D. I., and Pollak, F. H., *Effect of dislocations on thermal conductivity of GaN layers*, Appl. Phys. Exp. 79, 4316-4318 (2001).

[14] Mamand, S. M., Omar, M. S., and Muhammed, A. J., *Calculation of lattice thermal conductivity of suspended GaAs nanobeams: Effect of size dependent parameters*, Adv. Mat. Lett. 3, 459-458 (2012).

[15] Florescu, D. I., Asnin, V. M., Pollak, F. H., Molnar, R. J., and Wood, C. E. C., *High spatial resolution thermal conductivity and Raman spectroscopy investigation of hydride vapor phase epitaxy grown n-GaN/sapphire (0001): Doping dependence*, J. Appl. Phys. 88, 3295-3300 (2000).

[16] Nahid A Jahan, Claus Hermannstadter, Hirotaka Sasakura, Thomas J Rotter, Pankaj Ahirwar, Ganesh Balakrishnan, Hidekazu Kumano, Ikuo Suemune, *Carrier dynamics and photoluminescence quenching mechanism of strained InGaSb/AlGaSb quantum wells*, J. Appl. Phys. 113 (5), 053505-053505-7, (2013).

[17] P Ahirwar, D Shima, TJ Rotter, SPR Clark, SJ Addamane, CP Hains, LR Dawson, G Balakrishnan, R Bedford, YY Lai, A Laurain, J Hader, JV Moloney, *TEM based analysis of III-Sb VECSELs on GaAs substrates for improved laser performance*, SPIE LASE, 86060E-86060E-12, 2013.

Chapter 5

Conclusions and Future Directions

The design, epitaxial growth, characterization and performance analysis of III-Sb VECSELs grown on GaAs/AlGaAs DBRs have been discussed in this dissertation. The motivation for VECSELs operating at near 2μm wavelength was highlighted in Chapter 1 of this dissertation. Several applications can benefit from high output power VECSELs operating in this wavelength range. The III-Sb VECSELs are however unable to match the output power scaling similar to III-As based VECSELs due to the thermal management issues. The GaSb substrates on which these are grown have poor thermal conductivity. One of the proposed solutions to overcome this thermal bottleneck is to grow the III-Sb VECSEL active regions on GaAs substrates.

Chapter 2 discusses the VECSEL device physics and design of the components of a VECSEL. The operating principles of semiconductor lasers and benefits of a vertical emission geometry over an edge emitting are elaborated. VECSELs combine the benefits of a vertical emission geometry and high output powers. Linear external cavity design and mathematical formulation for parameters affecting the mode-size (on the VECSEL chip and output coupler) and cavity-stability are developed and

discussed. DBR design is one of the most important aspect of VECSEL design, the design parameters for 2 μm DBRs (using both III-As and III-Sb materials) are discussed. The physics of the quantum well gain regions, choice of barrier, QW and clad layer materials for near 2μm operation and benefit of a RPG arrangement of QWs during subcavity design are discussed. Since the VECSEL devices are very sensitive to the operating temperature, an efficient thermal management scheme is essential to ensure that they can operate at high output power regimes. The pros and cons of various thermal management schemes are discussed. The III-Sb VECSELs grown on GaSb rely on transparent heat spreader bonded to top layer for extraction of heat generated during operation. The surface quality of III-Sb VECSELs is therefore a crucial parameter as the only viable option is to extract heat from these devices is through top bonded transparent heat spreaders, the surface quality not only depends on MBE growth parameters but external factors such as quality of GaSb substrates. The growth the III-Sb VECSELs on GaAs substrates will allow complete removal of substrate through use of good etch-stop layers and superior etch chemistry of III-As material system.

The ability to grow $\sim$ 7.8% mismatched GaSb layers on GaAs substrates and eventually grow III-Sb VECSEL active regions on GaAs/AlGaAs DBRs is explored in Chapter 3. The growth of GaSb on GaAs relies on the formation of an array of 90° misfit dislocations which relieve strain energy at the interface. The key factors affecting the formation of such interface reliably and over large areas is discussed in detail along with probable failure mechanisms. The MBE growth and optimization of III-Sb VECSEL active regions are then discussed, the quality of III-Sb active regions is analyzed using PL and XRD. Active regions are designed for emission near 2μm and optimized for parameters such as growth temperature, indium composition in the quantum well, Sb-overpressure during growth of the active regions etc. The growth parameters of III-Sb VECSEL subcavity on the MOCVD grown DBRs are also optimized. The active regions and DBRs for III-Sb VECSELs on GaSb sub-

strates are also optimized. The grown structures are characterized using nomarski for surface quality and TDR for alignment of gain-subcavity. The VECSELs are designed such that the gain and subcavity resonance are offset at room temperature and align at about ∼353K. The gain-peak is about 40-50 nm shorter than the subcavity resonance peak. The alignment of gain-peak and subcavity resonance depends on thickness of subcavity structure and PL-emission from the QWs. The thickness variations can be estimated for a sample and corrected in the next epitaxial growth of the VECSEL subcavity.

The pulsed and CW lasing characterization of the grown VECSEL samples are discussed in detail in Chapter 4. The lattice matched VECSEL samples grown on GaSb outperform the lattice mismatched VECSEL samples in all lasing (CW and Pulsed) characteristics such as slope efficiency , maximum CW output power and threshold. From the rate-equation based analysis of the LMM-VECSEL samples it is speculated that the non-radiative recombination processes are dominant loss mechanisms in these structures. These losses limit the maximum CW output power from LMM-VECSELs to few 100's of mW when compared to LM-VECSEL which can operate at much higher CW output power levels (∼ 3W CW). On cross-section TEM investigation of LMM-VECSEL samples, threading dislocations with a TDD $10^8 \mathrm{cm}^{-2}$ are observed in their active regions. It is however observed that the TDD decreases as the distance from the mismatched interface is increased. It is also shown theoretically that the thermal conductivity of the semiconductor material can decrease with an increasing TDD. The carrier lifetime measurements are performed for III-Sb active regions grown on GaAs substrates with and without IMF interface. It is clear from these measurements that the threading dislocations play an important role in determining the carrier lifetime of excited carriers, and could also lead to PL quenching in active regions with high threading dislocation densities. Hence time-resolved PL measurement is an effective technique to determine the quality of IMF interface and can be used as a method to optimize performance of III-Sb active

regions. Another technique for reduction of threading dislocations in III-Sb active regions is to place the active regions farther away from the IMF interface. A III-Sb DBR is grown on GaAs substrate and within 3 μm from the IMF interface the TDD reduce from 10^9cm^{-2} to 10^7cm^{-2}. The placement of the III-Sb active region on top of this III-Sb DBR grown on GaAs substrate serves two purposes;

- IMF interface can be formed reliably on the GaAs substrate when compared to MOCVD grown III-As DBR
- The DBR acts as defect filtering layer and TDD significantly reduces towards the top layers of the III-Sb DBR grown on GaAs substrate

In future III-Sb VECSEL active regions can be grown on top of such III-Sb DBRs which are grown on GaAs substrates, also as the interface is farther away from the active region defect filtering layers such as GaSb/AlSb digital alloys can be placed immediately after the IMF interface for further reduction of TDD.